

# 1 The substorm cycle as reproduced by global MHD 2 models

E. Gordeev<sup>1</sup>, V. Sergeev<sup>1</sup>, N. Tsyganenko<sup>1</sup>, M. Kuznetsova<sup>2</sup>, L. Rastätter<sup>2</sup>,

J. Raeder<sup>3</sup>, G. Tóth<sup>4</sup>, J. Lyon<sup>5</sup>, V. Merkin<sup>6</sup> and M. Wiltberger<sup>7</sup>

3 CCMC GMHD models with same input (2h north - 2h south IMF Bz) compared to empiric  
4 duration and intensity of magnetotail loading/unloading

5 Three CCMC global MHD models show systematically different dynamics and different magnetic  
6 flux transfer characteristics

7 LFM results most closely resemble "idealized substorm"; BATSRUS and OpenGGCM rather  
8 show a smooth transition between two quasi-steady states

Author Manuscript

---

Corresponding author: Evgeny Gordeev, Saint-Petersburg State University, St. Petersburg,  
Russia (evgeny.i.gordeev@spbu.ru).

<sup>1</sup>Saint-Petersburg State University,

**This is the author manuscript accepted for publication and has undergone full peer review but has not been through the copyediting, typesetting, pagination and proofreading process, which may lead to differences between this version and the Version of Record. Please cite this article**

as doi: [10.1002/2016SW001495](https://doi.org/10.1002/2016SW001495) February 12, 2017, 1:51am

D R A F T

9 **Abstract.** Recently *Gordeev et al.* [2015] suggested a method to test global  
10 MHD models against statistical empirical data. They showed that four community-  
11 available global MHD models supported by the Community Coordinated Mod-  
12 eling Center (CCMC) produce a reasonable agreement with reality for those  
13 key parameters (the magnetospheric size, magnetic field and pressure) that  
14 are directly related to the large-scale equilibria in the outer magnetosphere.

St. Petersburg, Russia

<sup>2</sup>NASA Goddard Space Flight Center,  
Greenbelt, MD, USA

<sup>3</sup>Space Science Center, University of New  
Hampshire, Durham, NH, USA

<sup>4</sup>Center for Space Environment  
Modelling, University of Michigan, Ann  
Arbor, MI, USA

<sup>5</sup>Department of Physics and Astronomy,  
Dartmouth College, Hanover, NH, USA

<sup>6</sup>Applied Physics Laboratory, John  
Hopkins University, Laurel, MD, USA

<sup>7</sup>High-Altitude Observatory, National  
Center for Atmospheric Research, Boulder,  
CO, USA

15 Based on the same set of simulation runs, here we investigate how the mod-  
16 els reproduce the global loading-unloading cycle. We found that in terms of  
17 global magnetic flux transport, three examined CCMC models display sys-  
18 tematically different response to idealized 2h north then 2h south  $IMFBz$   
19 variation. The LFM model shows a depressed return convection and high load-  
20 ing rate during the growth phase as well as enhanced return convection and  
21 high unloading rate during the expansion phase, with the amount of loaded/unloaded  
22 magnetotail flux and the growth phase duration being the closest to their  
23 observed empirical values during isolated substorms. Two other models ex-  
24 hibit drastically different behavior. In the BATS-R-US model the plasma sheet  
25 convection shows a smooth transition to the steady convection regime after  
26 the IMF southward turning. In the Open GGCM a weak plasma sheet con-  
27 vection has comparable intensities during both the growth phase and the fol-  
28 lowing slow unloading phase. We also demonstrate potential technical prob-  
29 lem in the publicly-available simulations which is related to post-processing  
30 interpolation and could affect the accuracy of magnetic field tracing and of  
31 other related procedures.

## 1. Introduction

32 The Earth's magnetosphere provides a great challenge for researchers because of its inho-  
33 mogeneous, structured and extremely variable nature. Numerical simulations provide the  
34 only opportunity to follow the complicated evolution of the entire complex system, con-  
35 trolled by its ever-changing multi-parametric driver, the solar wind. Of all the available  
36 first-principle based approaches, the global MHD (GMHD) models have a special place  
37 due to their ability to simulate the entire solar wind driven magnetosphere at a low com-  
38 putational cost. However, because of their neglect of the kinetic aspects, they are unable  
39 to correctly describe the drift-dominated inner magnetosphere, as well as such impor-  
40 tant details of the systems response as the substorm onset time and location [*Kuznetsova*  
41 *et al.*, 2007]. There were attempts to incorporate a more sophisticated physics into the  
42 GMHD model, e.g., by locally including particle effects into the large-scale GMHD de-  
43 scription of the system [*Toffoletto et al.*, 2005; *Pembroke et al.*, 2012; *Daldorff et al.*, 2014;  
44 *Ashour-Abdalla et al.*, 2015]. However, none of them provided a cost-effective solution to  
45 replace the GMHD models for operational purposes and community-available research.  
46 Also, the addition of particle physics does not always improve the results of testing the  
47 models against data [*Pulkkinen et al.*, 2011; *Honkonen et al.*, 2013]. In addition, the  
48 GMHD simulations by themselves are still far from being a routine tool: there exist a  
49 dozen of different models worldwide and, quite often (see examples below) they provide  
50 widely different results on the system behavior and its parameter values. Therefore, the  
51 quantitative assessment and validation of the MHD component of global magnetospheric  
52 models against the reality still remains a critical but difficult issue.

53 Dozens of particular validation studies have been published so far. However there exists  
54 no commonly accepted optimal methodology how to compare the GMHD models against  
55 the reality. Most of the past validation attempts were separately applied to particular solar  
56 wind conditions or to particular magnetospheric parameter(s) measured at some particular  
57 locations. Recently *Gordeev et al.* [2015] (referred henceforth as G15) suggested a different  
58 procedure of the model benchmarking and tested it on four community-available GMHD  
59 codes operated by the NASA Community Coordinated Modeling Center (CCMC). The  
60 basic components of that approach are as follows. (1) Evaluate principal global variables  
61 (the state parameters, or key magnetospheric parameters) that quantitatively characterize  
62 the most important elements of the system structure and dynamics, and compare their  
63 model values with observations; (2) Use statistical empirical relationships to validate the  
64 model predictions, rather than observations along particular spacecraft orbits made at  
65 specific times; (3) Cover the most probable ranges of the solar wind input parameter  
66 values and avoid basing the metrics on regions or phenomena which (by their nature and  
67 the simulation design) are inaccurately reproduced by the GMHD model (e.g., the in-  
68 ner magnetosphere, ionospheric currents, ground magnetic perturbations, etc). Using of  
69 quantitative scores in a carefully designed statistical comparison of model predictions and  
70 observations provides an objective quantitative measure of a particular models perfor-  
71 mance. The G15 results have confirmed that all the GMHD models operated at CCMC  
72 (BATS-R-US, LFM, Open GGCM and GUMICS) are able to simulate the large-scale  
73 magnetospheric structure. They reasonably well predict the absolute values and aver-  
74 age SW-induced variations for those key parameters that characterize the magnetospheric  
75 size, magnetic field/flux, and plasma pressure in the tail. These global parameters are

76 directly related to the large-scale magnetospheric equilibria in the outer magnetosphere,  
77 which is supposed to be correctly described by the MHD approach. At the same time,  
78 the results for some other parameters, such as the global convection, total field-aligned  
79 current, or the magnetotails ability to store the magnetic flux after the north-south IMF  
80 turning, provided very diverse answers among four models. In this paper, we use the  
81 same set of simulations (except for GUMICS simulations) and focus on the ability of the  
82 models to reproduce the most important aspects of magnetospheric dynamics: the mag-  
83 netic flux transfer and the substorm-related loading-unloading cycle, which represents a  
84 principal large-scale perturbation in the magnetosphere and has important space weather  
85 implications [McPherron, 1991].

86 A fundamental concept in the large-scale magnetospheric dynamics is the magnetic flux  
87 circulation scheme, proposed by *Dungey* [1961] and further extended to non-steady state  
88 by *Russell and McPherron* [1973], *Semenov and Sergeev* [1981], *Siscoe and Huang* [1985],  
89 *Cowley and Lockwood* [1992], and many others, in application to the substorm process.  
90 Many observations in different magnetospheric domains have demonstrated the validity of  
91 the global circulation paradigm and the loading-unloading substorm cycle. Those include  
92 the magnetotail magnetic field measurements [*Russell and McPherron*, 1973; *Baker et al.*,  
93 1996; *McPherron*, 1991; *Shukhtina et al.*, 2005; *Angelopoulos et al.*, 2013] as well as in  
94 the ionospheric observations of convection patterns and polar cap size change [*Provan*  
95 *et al.*, 2004; *Milan et al.*, 2007; *DeJong et al.*, 2009; *Clausen et al.*, 2013]. Recently, the  
96 combined measurements of GPS receivers and SuperDARN radars made it possible to  
97 trace the entire Dungey cycle by having observed the convection of plasma irregularities  
98 in the high latitude ionosphere [*Zhang et al.*, 2015].

99 According to the concept of non-stationary Dungey cycle, different magnetospheric  
100 states result from the imbalance between the dayside and nightside reconnection rates.  
101 In particular, during the substorm growth phase the dayside reconnection rate is much  
102 larger than the nightside one [*Milan et al.*, 2007], which results in accumulation of the  
103 magnetotail magnetic flux ( $F_T$ ), current sheet thinning and overall stretching of the tail  
104 configuration [*Baker et al.*, 1996]. The net  $F_T$  increase by the end of the growth phase cor-  
105 responds to the amount of the magnetic flux that may be potentially reconnected during  
106 the substorm expansion phase, when the nightside reconnection rate abruptly increases  
107 and exceeds the intake rate on the dayside, resulting in the  $F_T$  reduction [*Yahnin et al.*,  
108 2006; *Milan et al.*, 2007; *Shukhtina et al.*, 2014]. Complementary to the magnetotail mag-  
109 netic flux (global parameter, which is relatively easy to monitor in the GMHD simulations)  
110 are the electric potential drops, which provide information about the global flux transport  
111 (and dissipation) rates in different parts of the magnetosphere. Combining these global  
112 state parameters allows us to quantitatively characterize the global flux transfer in the  
113 GMHD models. From four GMHD models supported by the CCMC (BATS-R-US [*Powell*  
114 *et al.*, 1999; *Tóth et al.*, 2012], Open GGCM [*Raeder et al.*, 2008], LFM [*Lyon et al.*, 2004;  
115 *Merkin and Lyon*, 2010], and GUMICS [*Janhunen et al.*, 2012]) - only the first three have  
116 been tested in this work. As detailed in G15, the GUMICS model was found to provide  
117 much lower flux transport and loading rates than other models for this particular set of  
118 low resolution simulations (see the lobe magnetic field and cross polar cap potential drop  
119 values and variations in Figs. 1 and 8 in G15, which can serve as indicators of magnetic  
120 flux transport behavior in the system), and this is why it was not included in the present  
121 study.

## 2. The set of simulations and computation of global parameters

122 In this study we use the same set of artificial event simulations as described in [*Gordeev*  
123 *et al.*, 2015]. The global numerical models solve similar system of ideal MHD equations,  
124 but they may significantly differ in numerical implementation details the type and order  
125 of numerical scheme, type of spatial grid, boundary conditions and others. A summary  
126 of the main characteristics of GMHD models used in our study can be found in the sup-  
127 plementary Table S1. The simulations have been done for comparable (medium) grid  
128 resolution (e.g. in the plasma sheet at  $X = -10R_E$ : BATS-R-US -  $0.25R_E$ , GUMICS -  
129  $0.5R_E$ , LFM -  $0.8R_E$ , Open GGCM -  $0.3R_E$ , see more details in the supplementary Table  
130 S1) and also tested with more fine grids, with no dipole tilt and constant ionospheric  
131 conductance, using the same set of inputs for all four GMHD models. A set of 19 IMF  
132 input sequences was devised, each containing 2h-long northward IMF interval followed by  
133 2h-long southward IMF interval - see an example in Fig. 2 later in the paper. All other  
134 SW parameters were fixed during each particular 4h-long simulation, but their values (as  
135 well as the amplitudes of northward and southward IMF) varied between different simu-  
136 lations to reproduce the statistical distribution of main solar wind driver variables, such  
137 as SW dynamic pressure and SW electric field. The supplementary Table S2 provides all  
138 SW/IMF input parameters as well as the names of corresponding runs, which can be found  
139 in the CCMC database [<http://ccmc.gsfc.nasa.gov/>]. Such a design of synthetic inputs  
140 has several advantages. First, it allows one to cover the actual range of many SW/IMF  
141 input parameters (and explore their effects) at relatively low computational costs. Second,  
142 the northward-then-southward IMF sequence represents the well-known condition leading  
143 to substorms [*McPherron*, 1991; *Baker et al.*, 1996; *Milan et al.*, 2007], so this simulation



144 set allows us to investigate the generation of substorm loading/unloading sequence for  
145 different values of input parameters, including different levels of northward  $Bz$ , plasma  
146 pressure and velocity prior to the event. The time resolution of the GMHD output was  
147 chosen as high as 1min during the first hour of southward IMF in each simulation (and  
148 5min in the rest of simulation) which allows an accurate timing of magnetotail changes  
149 to be made during the GMHD substorm.

150 A cornerstone of G15 validation approach is to investigate statistically the global key  
151 variables, which characterize the large-scale magnetospheric state and dynamics, rather  
152 than to study some particular parameters observed along specific orbits for particu-  
153 lar events. This allows us to concentrate on most essential and principal character-  
154 istics/processes of global scale and significance. For the MHD description (frozen-in  
155 plasma), which is expected to be valid in the outer magnetosphere, magnetosheath and  
156 solar wind, the magnetotail magnetic flux and global flux transport rate represent such  
157 natural global variables.

158 To identify and quantitatively characterize the substorm cycle in the simulations, we  
159 use the total magnetic flux in the magnetotail ( $F_T$ ). As a traditional measure of the  
160 global convection strength we use the cross polar cap electric potential ( $CPCP$ ) in the  
161 ionosphere, which is routinely provided by the CCMC tools and represents the difference  
162 between the maximum and minimum values of the electric potential in the high-latitude  
163 ionosphere (here, in the northern hemisphere). As shown in *Gordeev et al.* [2011] the  
164  $CPCP$  is basically contributed by the dayside merging integral rate, therefore it can serve  
165 as a proxy of the dayside merging key parameter. As a measure of the flux transport rate  
166 in the plasma sheet, a cross-tail electric potential in the tail plasma sheet ( $CTP$ ) was

167 calculated in the  $X = -15R_E$  magnetotail cross-section by integrating the electric field  
 168  $(E = -V \times B)$   $y$ -component in the equatorial plane, the integration was performed along  
 169 the  $Y$  axis between  $Y = -15R_E$  and  $Y = +15R_E$ , that is

$$CTP = - \int_{-15}^{+15} (\mathbf{V} \times \mathbf{B})_y dy \quad (1)$$

170 As an integral measure of the magnetic flux transport along the tail, the  $CTP$  parameter  
 171 was found to only weakly depend on  $X$ , i.e., to be insensitive to the location of the  
 172 reconnection line. We have quantitatively verified and confirmed that fact at a set of  
 173 locations between  $X = -12$  and  $-25R_E$ .

174 The  $F_T$  value is calculated in the same  $YZ$  tail cross-section at  $X = -15R_E$  by integrat-  
 175 ing the magnetic field  $x$ -component in the tail cross-section confined by the magnetopause  
 176 and equatorial plane, that is

$$F_T = - \int_S B_x ds \quad (2)$$

177 The distance  $15R_E$  is the optimal choice, since here the configuration is tail-like and the  
 178 grid resolution in the models is still good compared to larger distances.

179 A critical part of the  $F_T$  calculation is the magnetopause identification. It can be  
 180 defined in the simulated magnetosphere by finding either the peak of electric current, or  
 181 the maximum of plasma density (or thermal pressure) gradient, or using the combination  
 182 of these two [Garcia and Hughes, 2007]. These methods are computationally cheap,  
 183 but they usually fail at low latitudes where the field and plasma gradients are more  
 184 distributed and structured. Following Palmroth *et al.* [2003], in most of recent studies

185 [*Gordeev et al.*, 2011; *Wang et al.*, 2014a] the authors identified the GMHD magnetopause  
186 as the fluopause surface, i.e., the innermost boundary of the plasma streamlines coming  
187 from the solar wind and enclosing the magnetospheric cavity. The fluopause method  
188 is robust and it gives a smooth magnetopause proxy in both high and low latitudes.  
189 However, in our experience, the fluopause may have difficulties related to the nonlocal  
190 nature of the method: while moving along the magnetosheath, the solar wind plasma also  
191 penetrates into the magnetosphere, thus giving rise to the plasma mantle, which is located  
192 inside the lobes, convects inward, and eventually reaches the plasma sheet somewhere at  
193 distances  $\sim 60-150R_E$  [*Pilipp and Morfill*, 1978; *Wang et al.*, 2014b]. From the viewpoint  
194 of computational costs, the fluopause method is quite expensive, as it usually requires to  
195 trace thousands of streamlines at each step.

196 In this paper, to find the magnetopause we use a different approach. As suggested by  
197 *Peng et al.* [2010] and confirmed in our extensive testing using big simulation data set for  
198 3 GMHD models, the locations where the particle mass flux ( $mNV$ ) is reduced to half of  
199 its initial value in the solar wind can be considered as a good proxy for the magnetopause  
200 position. That simple method is based on the basic MHD variables, does not require to  
201 compute derivatives or trace the flowlines, is local, computationally cheap, and gives a  
202 smooth and well-defined surface whose location is in a good agreement with other local  
203 methods - see Fig. 1b for the illustration and Appendix 1 for more details on the method  
204 and its comparison to other methods.

205 Three above defined global variables help us control the global magnetic flux transport  
206 in the system and identify the GMHD analogies for the substorm phases. As discussed  
207 by *Semenov and Sergeev* [1981] and *Siscoe and Huang* [1985], the magnetic flux variation

in the tail cross-section obeys the Faraday law, which gives a simple relationship for a  
 contour  $abcd$  encircling the northern half of the tail cross-section as shown in Figure 1a:

$$dF_T/dt = \Phi_{MP} - \Phi_{PS} \quad (3a)$$

$$\Phi_{MP} = \int_{abc} \mathbf{E} \cdot d\mathbf{l} = - \int_{abc} [\mathbf{V} \times \mathbf{B}]_t dl \quad (3b)$$

$$\Phi_{PS} = \int_{aac} E_y dy \quad (3c)$$

Here the electric field circulation along the closed contour is split into two parts. One  
 part ( $\Phi_{MP}$ ) integrates tangential  $E$ -field along the magnetopause from dawn to dusk,  
 it represents a solar wind dynamo, indicating magnetic flux transport from the dayside  
 magnetosphere into the magnetotail. We may think of cross-polar cap potential in the  
 ionosphere ( $CPCP$ ) as a proxy of dayside reconnection potential in the simulations [*Siscoe*  
*et al.*, 2004; *Gordeev et al.*, 2011]. Another part ( $\Phi_{PS}$ ) represents an integral measure of  
 the plasma sheet convection and is roughly proportional to the total dissipation rate  
 ( $\int E_y J_y dy$ ) in the plasma sheet. Its proxy in our simulation is provided by the  $CTP$   
 parameter.

### 3. Large scale dynamics observed in the GMHD simulations

Figure 2 illustrates the simulated behavior of  $F_T$ ,  $CTP$  and  $CPCP$  global variables  
 observed in three GMHD models for two different input sequences (#3 and #8), which  
 both have a comparable solar wind merging  $E$ -field ( $E_{KL} = V_{SW} B t_{SW} \sin^2(\theta/2)$  of  $\sim$   
 3 mV/m) and are expected to have similar loading-unloading rates. An obvious conclusion  
 is that three GMHD codes provide systematically different magnetospheric reaction under  
 the same driver intensity. In particular, the amount of magnetic flux in the tail and the

225 level of magnetospheric and ionospheric convection may differ by several times between  
 226 the models. Also there are visible differences in the dynamics of their behavior after the  
 227 southward turning of IMF at  $t = 120$  min. An example of time sequence of meridional  
 228 and equatorial views of the magnetic field, flow pattern, pressure and flux transport in  
 229 these three models is presented in supplementary movies.

230 A simple picture based on eq. (3) and Fig. 1a is useful as a guide in our efforts to identify  
 231 the GMHD substorm. In the case of idealized sequence of the IMF variation, the first  
 232 2-hour-long time interval of northward IMF is expected to provide a quiet presubstorm  
 233 background, with low  $\Phi_{MP}$  (*CPCP*),  $\Phi_{PS}$  (*CTP*) and  $dF_T/dt$ , which is the case in all  
 234 examples shown in Figure 2. Following after the arrival of southward IMF to the subsolar  
 235 magnetopause and enhancement of the dayside reconnection, one expects (and observes,  
 236 see Fig. 2) the *CPCP* growth and associated increase of  $\Phi_{MP}$ , implying the loading of  
 237 the reconnected flux tubes to the magnetotail. The actual behavior of  $dF_T/dt$  depends  
 238 on the balance between the loading of the flux tubes into the lobes from dayside  $\Phi_{MP}$   
 239 and the plasma sheet convection rate  $\Phi_{PS}$  which returns the plasma tubes back to the  
 240 dayside. The most effective loading during the growth phase is expected in the case of  
 241 no convection ( $\Phi_{PS} = 0$ ) when all the loaded magnetic flux is accumulated in the tail, so  
 242 that  $dF_T/dt = \Phi_{MP}$  [*Semenov and Sergeev, 1981*]. In terms of our variables, this should  
 243 correspond to the situation of low *CTP* and fast  $F_T$  growth, which appears to be realized  
 244 in LFM simulations (blue curves in Fig. 2). In case of strongly enhanced plasma sheet  
 245 convection and dissipation ( $\Phi_{PS} > \Phi_{MP}$ ), one expects to see the unloading of the tail  
 246 flux ( $dF_T/dt < 0$ ). This is usually associated with enhanced reconnection in the mid-tail  
 247 region, accompanied by many other related dissipative phenomena which in combination

248 characterize the substorm expansion phase. Such contrasted behavior of the plasma sheet  
249 convection during the growth and expansion phase of substorms is systematically observed  
250 in the mid-tail plasma sheet [*Nakamura et al., 1999; Dmitrieva et al., 2004*]. In these  
251 examples, the LFM simulation provides the most contrasting example of substorm phases  
252 in the *CTP* parameter. Let us examine the outputs of three models in more detail.

253 A sharp increase of the ionospheric convection (*CPCP*) after  $t = 120$  min is seen in  
254 all models but with different amplitudes. The *CPCP* amplitude is close to its empirical  
255 values in BATS-R-US and is enhanced by a factor of 2 and 2.5 in LFM and Open GGCM  
256 models respectively (see statistical results in Fig. 8 of G15). The magnetic flux enhance-  
257 ments during the substorm growth phase differ significantly between the models both in  
258 their duration and amplitude.  $F_T$  increases by about a factor of 3 (from 0.27 GWb to  
259 0.74 GWb) during 45 minutes in the LFM model, while it gains  $\sim 40\%$  (0.39 GWb to  
260 0.60 GWb) during a short 30-minute growth phase in the BATS-R-US model. In its turn,  
261 the Open GGCM starts from twice higher  $F_T$  (0.53 GWb) and within 70 minutes increases  
262 the amount of the lobe flux by  $\sim 60\%$  to 0.84 GWb.

263 Examination of the cross-tail potential complements the interpretation of the tail flux  
264 variations. Contrary to the expected depressed plasma sheet convection during the growth  
265 phase, in Open GGCM simulations the *CTP* increases to several tens of kV in several  
266 minutes after the start of the magnetic flux loading to the tail or even prior to it. After that  
267 it continues to rise together with  $F_T$ , indicating the enhanced convection and dissipation  
268 in the plasma sheet. In the BATS-R-US simulations the *CTP* steadily increases soon  
269 after the start of  $F_T$  loading and in  $\sim 25$  minutes after that it reaches the level of several  
270 tens of kV, corresponding to the peak strength of plasma sheet convection and dissipation

271 attained during the simulation. In both the models, the obtained variations resemble  
272 the smooth transition between two quasi-steady states. After a weak enhancement, the  
273  $CTP$  value in all the LFM simulations remains suppressed at low level (compared to  
274  $CPCP$ ) during the growth phase, until its sharp increase which indicates the start of the  
275 expansion phase (here the  $CTP$  values are several times larger than the  $CPCP$  level)  
276 closely resembling the idealized substorm behavior as described by *McPherron* [1991],  
277 *Baker et al.* [1996], *Shukhtina et al.* [2005] and *Milan et al.* [2007].

278 Now we compare quantitatively the global behavior with the empirical data. This is not  
279 a simple task because both the  $F_T$  and  $CTP$  variables are not directly measurable, so no  
280 empirical relations are available for them. For that purpose we use two related character-  
281 istics, both characterizing the global system behavior. One of them is the duration of the  
282 growth phase. From simulations, the growth phase onset time  $T_s$  is defined as the start  
283 time of lobe magnetic field increase, and the growth phase end (or expansion onset) time  
284  $T_e$  is defined by the time when  $B_L$  reaches its maximum, thus giving  $T_{GP} = T_e - T_s$ . From  
285 observations (see Appendix 2 for more details), during isolated substorms  $T_s$  is identified  
286 as the onset of polar cap convection ( $PC$ -index) growth, whereas the expansion onset  
287 time  $T_e$  is taken from sudden intensification of the auroral zone westward electrojet (of  
288 the  $SML$ -index, see [*Newell and Gjerloev, 2011*]). Comparison of modeled and empirical  
289 growth phase durations as a function of solar wind-induced merging electric field ( $E_{KL}$ )  
290 is presented in Figure 3a.

291 Another useful characteristic of the loading rate is provided by the variations of the  
292 lobe magnetic field  $B_L(t)$  taken at the reference point  $(-15,0,10)R_E$ . In the model we  
293 define the lobe field increase rate as the difference of  $B_L$  values taken at the times close to

294  $T_e$  and  $T_s$ , divided by this duration (that is  $dB_L/dt = (B_e - B_s)/T_{GP}$ ). For comparison  
 295 we need the statistical empirical relationship of  $dB_L/dt$  reduced to the reference point  
 296 and expressed as a function of the solar wind electric field. Since no such relationship  
 297 was available from previous studies (except from that of *Rybalchenko and Sergeev* [1985]),  
 298 this was derived from analyses of the lobe magnetic field measurements combined with the  
 299 OMNI data base solar wind data (see Appendix 2 for the information about the procedure  
 300 and results). Comparison of modeled and empirical loading rates as a function of solar  
 301 wind electric field ( $E_{KL}$ ) is presented in Figure 3b for the lobe magnetic field.

302 The range and distribution of empirical  $T_{GP}$  values in Fig. 3a as well as their decreasing  
 303 trend with the increasing  $E_{KL}$  magnitude are similar to those found in previous studies  
 304 [*Dmitrieva and Sergeev*, 1983; *Petrukovich*, 2000; *Li et al.*, 2013]. The LFM model clearly  
 305 reproduces the  $T_{GP}$  dependence on  $E_{KL}$ , while there is a strong scatter in the Open GGCM  
 306 output. The growth phase duration in both MHD models is typically by  $\sim 20\text{-}30\%$  shorter  
 307 than the average empirical values. In the BATS-R-US model the loading duration is short  
 308 ( $\sim 25$  min) and almost independent on  $E_{KL}$ .

309 As concerns the lobe magnetic field increase rate during the growth phase, all models  
 310 show its growth with the increase of dayside merging rate proxy  $E_{KL}$  as required by the  
 311 Faraday law in eq. (3). Compared to empirical estimates, the LFM provides a  $\sim 30\text{-}40\%$   
 312 larger  $B_L$  increase, it compensates the shorter growth phase duration and may provide  
 313 the realistic total loaded flux. In Open GGCM the growth rate is  $\sim 30\%$  smaller than  
 314 the empirical estimate, so the total loaded flux should be somewhat underestimated.  
 315 The BATS-R-US model provides the loading rate only slightly higher than empirical but  
 316 similarly should underestimate the loaded flux because of very short loading duration.



317 As concerns the unloading stage, three models show some unloading during a 2h south-  
318 ward IMF direction simulation interval, but again it show significant differences. There  
319 are distinct discrepancies in the onset  $F_T$  value, unloading rate and duration and, conse-  
320 quently, the amount of magnetic flux removed from the tail. Two artificial events shown  
321 in Fig. 2 demonstrate very modest flux unloading in Open GGCM simulations (from 0.85  
322 to 0.75 GWb, 12%, and from 0.76 to 0.69 GWb, 9%), and in the BATS-R-US simulations  
323 (from 0.60 to 0.55 GWb, 8%, and from 0.66 to 0.59 GWb, 11%). However, the flux re-  
324 moval is much larger in the LFM simulations (from 0.73 to 0.50 GWb, or 32%, and from  
325 0.81 to 0.59 GWb, 27%). There are also significant quantitative and qualitative differ-  
326 ences between models concerning the level and appearance of the plasma sheet convection  
327 in the plasma sheet, this will be discussed at more length in the next section.

#### 4. Average behavior of global variables

328 To characterize statistically the global behavior and to compare average parameters of  
329 magnetic flux loading/unloading with their previously published estimates, we present the  
330 superposed epoch analysis for 19 GMHD substorms. As a reference point to construct the  
331 Figure 4 we use the time of the tail flux peak at  $X = -15R_E$ . In a visual way these results  
332 reveal significant and systematic differences in the behavior of the tail magnetic flux and  
333 plasma sheet convection as described by three GMHD models. The large contrast between  
334 the growth and expansion phases is present in the LFM simulations: in that model the  
335 plasma sheet convection is significantly depressed/enhanced (roughly, the  $CTP$  is 30 kV  
336 and 280 kV), which is reflected in the largest rates of magnetic flux loading/unloading  
337 compared to other models. Quite differently, the Open GGCM shows that the plasma  
338 sheet convection and dissipation starts soon after the southward turning and continues

339 at roughly the same level throughout the growth and expansion phase (both at approx.  
340 100 kV for *CTP* average levels). It demonstrates the smallest contrast between two  
341 phases and the smallest average loading/unloading rates among the three models (see  
342 also Fig. 3b). In the BATS-R-US simulations, the growth phase has a shortest duration  
343 ( $\sim 25$  min, see also Fig. 3a), and during that time interval the plasma sheet convection is  
344 steadily increasing. In the BATS-R-US simulations there is no similarity to the behavior  
345 expected during substorms: there is very little unloading and the plasma sheet convection  
346 is not enhanced significantly during the expansion phase (after  $T = 0$ ) compared to the  
347 final growth phase; here the earthward convection (*CTP*) starts to grow steadily during  
348 the very short growth phase, as has been already discussed above.

349 Quantitatively, on the average the BATS-R-US model shows the flux unloading from  
350 0.60 to 0.57 GWb (5%) during the first 15 minutes after  $T = 0$ , with no change afterwards.  
351 Average tail flux unloading in Open GGCM starts from higher value of  $F_T = 0.77$  GWb,  
352 and the magnetic flux decreases to 0.71 GWb (8%) during next 60 minutes. In the LFM  
353 simulation during  $\sim 50$  min. long substorm expansion, the  $F_T$  decreases from 0.71 to  
354 0.49 GWb (31%); most of this unloading occurs during first 30 min after  $T = 0$ .

355 There are a few statistical studies of tail magnetic flux variations during substorms to be  
356 compared with the GMHD simulation results. Analyses of in situ evaluated magnetotail  
357 flux estimated using two-spacecraft based method [Shukhtina et al., 2016] demonstrates a  
358 41% magnetic flux decrease (from 0.82 to 0.48 GWb during  $\sim 60$  min.) for 110 substorm  
359 events [Shukhtina et al., 2014]. One should caution that selection of substorms in this  
360 study was based on intense unloading signature, so this may provide rather an upper esti-  
361 mate of the average change. Other statistical studies are based on the polar cap magnetic



384 An extended view of the global behavior is provided by Figure 5. In addition to magnetic  
 385 flux and plasma sheet convection in the tail it also includes the parameters routinely  
 386 evaluated at the ionospheric level at the CCMC, namely, the polar cap magnetic flux  
 387 ( $F_{PC}$ ) and the cross-polar cap potential ( $CPCP$ ). Comparison of the magnetic fluxes  
 388 generally shows qualitatively similar time variations of  $F_T$  and  $F_{PC}$ , however the  $F_{PC}$   
 389 amplitude is systematically larger than the  $F_T$  amplitude at the end of growth phase: the  
 390 average difference is about 40% for BATS-R-US and Open GGCM models, and it is about  
 391 10% for LFM. Such a large difference is a puzzle, its possible origins are discussed in the  
 392 next section.

393 Significant differences between different models are also evident when comparing the  
 394 ionospheric ( $CPCP$ ) and cross-tail ( $CTP$ ) potentials. In case of BATS-R-US model they  
 395 are of nearly the same magnitude (roughly 100 kV) and the increase in  $CTP$  potential  
 396 follows with  $\sim 25$  min. time delay after the  $CPCP$  increase, consistent with a short  
 397 25 min. growth phase in the lobe magnetic flux. The BATS-R-US actually yields a  
 398 smooth transition to a new balanced state, but with enhanced convection level (that is, a  
 399 steady convection event). The Open GGCM results are very different and unexpected: the  
 400 plasma sheet potential is 2-3 times smaller compared to the ionospheric potential (which  
 401 by a factor of  $\sim 3$  overestimates observational data, see Fig. 8 in G15 paper). Finally,  
 402 the LFM model displays, both qualitatively and quantitatively, a different relationship:  
 403 during the growth phase the  $CPCP$  increases up to  $\sim 150$  kV (still larger than in reality,  
 404 see Fig. 8 in G15 paper), while  $CTP$  remains at  $\sim 30$  kV level. As discussed before, this  
 405 situation ( $\Phi_{MR} \gg \Phi_{PS}$  in Fig.1a) provides the most effective loading of magnetic flux  
 406 into the tail. During the expansion phase, the relationship is opposite: here  $CTP$  jumps

407 by an order of magnitude and this situation ( $\Phi_{MP} \ll \Phi_{PS}$ ) provides effective unloading  
408 from the tail and enhanced convection and energy dissipation in the tail plasma sheet.

## 5. Discussion and concluding remarks

409 Global MHD models demonstrated their important role in Space Weather as an effi-  
410 cient physics based research and prediction tool. Substorms are an important part of  
411 Space Weather: they are significant contributors to the ring current and radiation belt  
412 populations [Chlioulidou et al., 2014; Jaynes et al., 2015] and a factor of central importance  
413 in the energetic particle precipitation into the ionosphere. Their diverse space weather  
414 applications were recently demonstrated to also include significant effects on the upper  
415 atmosphere [Causen et al., 2014] and even on the middle atmosphere, including ozone  
416 depletion [Seppala et al., 2015]. A very special role of substorms is due to high peak values  
417 of  $E$ -field generated during the unloading phase in the tail reconnection and BBF genera-  
418 tion processes, operated in localized parts of the magnetotail [Semenov and Sergeev, 1981;  
419 Baker et al., 1996]. These high (inductive)  $E$ -fields provide effective particle acceleration  
420 as well as their inward injection and precipitation [Birn et al., 2012]. Therefore, it is  
421 crucially important for Space Weather applications to find out how well the global MHD  
422 codes reproduce the loading-unloading cycle and large plasma sheet  $E$ -fields during the  
423 unloading phase.

424 One purpose of G15 and this paper was to demonstrate what a CCMC user would get  
425 after having launched an idealized simulation with 2 hours of northward IMF followed by  
426 2 hours of southward IMF using the CCMC Run on-request system? And also, are there  
427 systematic differences between the answers provided by different GMHD models with the  
428 same inputs? There was shown in G15 that four CCMC-supported GMHD models are

429 able, in general, to successfully reproduce the global magnetospheric equilibria in the wide  
430 range of input SW/IMF parameters. Here we emphasize, however, that a fundamental  
431 systematic difference exists in the dynamical response of these models to the same north-  
432 to-south IMF variation, aimed to simulate the loading-unloading sequence. We found the  
433 LFM manifest a clear difference between the substorm phases, with depressed convection  
434 in the tail plasma sheet during the growth phase and sharp (an order of magnitude)  
435 enhancement of convection level during the expansion phase, which fits to the classical  
436 substorm concept and agrees with experimentally observed magnetic flux changes during  
437 isolated substorms (Fig. 3). In contrast, in the BATS-R-US and Open GGCM simulations  
438 a gradual enhancement of the magnetotail convection starts from the very beginning  
439 of global convection cycle induced by southward IMF, so it rather resembles a smooth  
440 transition from the quiet state to steady magnetospheric convection. Such a different  
441 system behavior also results in a big quantitative difference in the basic global dynamical  
442 characteristics, such as the rate and amount of loaded and unloaded magnetic flux, and the  
443 duration of the growth and expansion phases. The difficulty of reproducing the transient  
444 response in BATS-R-US simulations has been previously noticed by *Kuznetsova et al.*  
445 [2007], who found that inclusion of nongyrotropic corrections is necessary to get the  
446 dynamic quasi-periodic response to the steady driving conditions. In this respect we  
447 emphasize once more, that our validation results characterize the pure MHD component  
448 of global models (without merged kinetic modules), and that in general, the incorporation  
449 of kinetic effects in some parts of the computation domain may certainly influence the  
450 system behavior.

451 One of important technical aspects of numerical modeling is the spatial resolution, which  
452 controls the numerical effects (such as the numerical diffusion) and can significantly affect  
453 the solution. In our approach we tried to run models at comparable resolution, but this  
454 appeared to be difficult to realize because of different grid organization in the models  
455 (see, e.g., supplementary Table S1). Also the time costs of the massive computations in  
456 this project forced us to set the medium resolution for all simulations. So the question  
457 of how the results are changed with the increasing grid resolution needs to be addressed.  
458 For this purpose, we performed the simulation run #02 with twice higher resolution for  
459 the LFM ( $106 \times 96 \times 128$  instead  $53 \times 48 \times 64$  cells) and Open GGCM (9M instead  
460 3.5M cells). Note, the BATS-R-US simulations were initially performed with the best  
461 spatial resolution routinely available at CCMC for that moment (2M cells). Comparing  
462 the high- and medium-resolution runs did not reveal any fundamental difference in the  
463 integral parameter values and behavior (Fig. 6). The high-resolution simulations in both  
464 LFM and Open GGCM models showed little difference in details of the loading-unloading  
465 sequence, and yielded a somewhat lower loading rates and slightly delayed times of the  
466 reconnection intensifications (which brings the LFM parameters somewhat closer to their  
467 experimental values, cf. Fig. 3).

468 Another critical point is the choice of ionospheric conductance model that can poten-  
469 tially affect the magnetospheric dynamics [Raeder *et al.*, 2001]. To validate our results,  
470 obtained from simulations with a flat ionospheric conductance, we performed an additional  
471 simulation of the runs #02 with "auroral model" of ionospheric conductance [Goodman,  
472 1995], which is dependent on UV solar irradiance as well as particle precipitation from the  
473 magnetosphere. The comparison shown in Figure 6 (Left) demonstrates virtually identi-

cal values and behavior of  $CPCP$ ,  $F_T$  and  $CTP$  parameters in BATS-R-US simulations with different ionospheric models. In the case of Open GGCM, the "auroral ionosphere" noticeably reduces the level of ionospheric and magnetotail convection in self-similar manner leaving the magnetotail flux changes at the same level. In the LFM simulation with "auroral conductance" the only change is the 10 min. earlier development of the substorm expansion as compared to the case with flat conductance.

Both spatial resolution and the ionospheric conductance model can modify the simulated magnetospheric response. However, the main global-scale dynamical features – the large difference between the average convection level during the growth and expansion phases in the LFM simulation, the absence of such a big difference in the Open GGCM simulations, and the smooth transition between two steady configurations in BATS-R-US – remain the same.

The large difference between the values and variation amplitudes of the polar cap ( $F_{PC}$ ) and tail ( $F_T$ ) magnetic fluxes in Fig. 5 is an unexpected result, which (to some extent) may influence the interpretation, so it also requires some explanation and discussion. Such a disagreement may have both natural (physics-related) reasons or be due to numerical artifacts. As concerns the natural reasons, the compared fluxes can indeed be different: the magnetic flux in the tail cross-section at  $X = -15R_E$  certainly include the flux closed at larger tailward distances (which nominally does not contribute to  $F_{PC}$ ), while, at the same time, the  $F_{PC}$  includes the newly reconnected (open) flux that permeates through the magnetopause between the cusp (say, at  $X = 0$ ) and the tail cross-section of interest (at  $X = -15R_E$ ), which is not counted in the  $F_T$  calculation and may increase  $F_{PC}$  in excess of  $F_T$ . This additional flux is readily evaluated as  $F_{rec} = \Phi_D \cdot \Delta X / V_{SW}$ ,



497 where  $\Phi_D$  is the dayside reconnection rate. Taking  $\Delta X = 15R_E$ ,  $V_{SW} = 400$  km/s,  
498 and  $\Phi_D = 100$  kV, the newly opened flux penetrating through the magnetopause is  
499  $F_{rec} = 10^5 \cdot (15 \cdot 6400)/400 = 0.024$  GW. This estimate is by an order of magnitude  
500 smaller than the difference between  $F_{PC}$  and  $F_T$  variations in Fig. 5 (being as large as  
501 0.2 GWb and 0.3 GWb for BATS-R-US and Open GGCM), so this reasoning can hardly  
502 explain the magnetic flux discrepancy in these models.

503 Other sources of the discrepancy between  $F_{PC}$  and  $F_T$  values can be related to some  
504 technical problems, such as precision of the boundary determination. First is a low preci-  
505 sion of magnetotail boundary determination when calculating tail magnetic flux, which is  
506 hardly to be the case if using the mass flux method (see more about it and its comparison  
507 to other methods in Appendix 1). The difference between the integrated tail magnetic  
508 flux, calculated using the magnetopause obtained from the mass flux method and from  
509 the fluopause method, rarely exceed 10% (which gives an upper estimate of  $F_T$  error due  
510 to inaccurate magnetopause determination).

511 The violation of  $divB = 0$  and resulting magnetic flux loss in the plasma tube (see  
512 Appendix 3) nominally should not contribute to the discussed discrepancy: OpenGGCM  
513 and LFM models exploit the constrained transport scheme to ensure that  $divB = 0$  con-  
514 dition is fulfilled automatically, the BATS-R-US model operated at CCMC includes some  
515 divergence cleaning tools to remove the unphysical part of the magnetic field accumu-  
516 lated during the simulation (we note, however, that user should ensure that this option  
517 is switched on at the Run-on-Request system by contacting CCMC staff). However, the  
518 second potential source of discrepancy is the magnetic field interpolation errors, which can  
519 influence the accuracy of magnetic field line mapping and the polar cap boundary location,

520 as well as some other post-processing procedures. Some evidence of that is presented in  
521 Appendix 3, demonstrating that computations using simple  $B$ -field interpolation meth-  
522 ods (which are also implemented at CCMC) results in unexpected effects like a magnetic  
523 flux loss/gain in the magnetotail magnetic flux tube, or generation of non-zero  $divB$ , etc.  
524 Such numerical artifacts may also influence the accuracy of a number of magnetic field  
525 -based post-processing procedures, like magnetic field line mapping, or flux tube volume  
526 and entropy calculation, as well as the determination of the polar cap boundary (which  
527 is defined as the ionospheric mapping of open/closed field line topological boundary) etc.  
528 As this may significantly impact the interpretation of GMHD data, this issue definitely  
529 needs attention of both developers and the CCMC.

530 The origin of the other discrepancy the above discussed large difference between the  
531 average ionospheric and plasma sheet electric potential drops in the Open GGCM simu-  
532 lation remains yet unclear. According to the Faradays law (eq. (3)), such a difference  
533 (average  $PCP \sim 200 - 300$  kV vs average  $CTP \sim 130$  kV, during post-onset intervals)  
534 should result in a considerable magnetic flux accumulation during both growth and ex-  
535 pansion phases, which is actually not observed in the simulations. Alternatively, such a  
536 discrepancy would require large (50 - 100 kV) potential drops along magnetic field lines,  
537 in order to electrically decouple the ionosphere from the magnetosphere.

538 As a final remark, we realize that, first, there can be a number of hidden adjusting  
539 parameters that control the codes performance and, second, the described problems may  
540 refer to only their publicly-available versions operated at the CCMC. However, we never-  
541 theless find it important to diagnose and discuss these issues from the users perspective.

542 To conclude, as a follow-up study to [Gordeev et al., 2015], we tested in this paper the  
543 ability of three community-available GMHD magnetospheric models operated by NASA  
544 CCMC to reproduce the fundamental and observationally well-established substorm-  
545 related global cycle of the magnetic flux loading-unloading, initiated by the southward  
546 turning of the IMF. Our main findings are as follows:

547 (1) Being tested with a comparable grid resolution and using the same set of 19 input  
548 sequences with north-to-south IMF turning, three CCMC-supported models displayed a  
549 systematically different global behavior. Among those models, the LFM displayed the  
550 generic substorm-like behavior of mutually-related tail magnetic flux variations ( $dF_T/dt$ ),  
551 the dayside merging-induced tailward convection (*CPCP*), and the return convection  
552 (*CTP*), as known from observations and summarized in phenomenological near-Earth  
553 neutral line model [McPherron, 1991; Baker et al., 1996], is most clearly manifested by the  
554 LFM model. Only for that model the return convection is depressed and the loading rate  
555 is high during the growth phase whereas the return convection is enhanced and unloading  
556 rate is high during the expansion phase. Quantitatively, the amount of loaded/unloaded  
557 magnetotail flux and the growth phase duration in the LFM were closest to their values  
558 empirically observed for the isolated substorms. Two other models showed a drastically  
559 different behavior, with the BATS-R-US plasma sheet convection exhibiting a smooth  
560 transition to the steady convection regime after the IMF southward turning, while the  
561 Open GGCM showed rather weak plasma sheet convection (*CTP* smaller than *CPCP*)  
562 with comparable intensities during the growth and expansion phases.

563 (2) Our investigation also identified potential problems in post-processing calculations  
564 based on the routinely interpolated values of simulated magnetic fields. This includes

565 a noticeable non-zero  $\text{div}B$  based on interpolated magnetic field and a loss of magnetic  
566 flux in the magnetic flux tube, signalling on the errors which may affect the accuracy  
567 of magnetic field tracing and calculation of such parameters as polar cap area, magnetic  
568 tube volume and others. Final evaluation of the severity of discovered problems as well  
569 as solving them is beyond the scope of our study as it will require concerted efforts on the  
570 part of the developers, CCMC staff and the users community.

571 **Acknowledgments.** This study was supported by Russian Science Foundation grant  
572 14-17-00072. The National Center for Atmospheric Research is supported by the National  
573 Science Foundation. Model computations were performed at the Community Coordinated  
574 Modeling Center, NASA GSFC, and all simulation results can be found in the CCMC  
575 database [<http://ccmc.gsfc.nasa.gov/>] under the names shown in the supplementary Ta-  
576 ble S2. The authors would like to acknowledge the CCMC staff for their generous support  
577 throughout the work described in this paper. The solar wind and activity indices were  
578 provided by the NASA CDAWeb and OMNIWeb sites. For the substorm onset list we  
579 gratefully acknowledge the SuperMAG initiative and the SuperMAG collaborators. We  
580 thank M. Kholeva for her help in the manuscript preparation.

## Appendix A: Fast computation of the simulated tail magnetopause and magnetic flux

581 To calculate the magnetic flux through the  $YZ$  cross-section of the magnetotail, one  
582 needs to integrate the  $X$ -component of the magnetic field over that section, that is, eval-  
583 uate  $F_T = \int B_x ds$ . To determine the magnetopause position, we use a fast and robust  
584 method by Peng *et al.* [2010], based on the particle mass flux. Its essence is to find  
585 a surface where the mass flux  $mNV$  becomes twice smaller than the solar wind mass

586 flux  $mN_{SW}V_{SW}$ . This simple procedure gives an adequate proxy for the tailward mag-  
587 netopause position. For illustration, we show the magnetopause proxies at  $X = -15R_E$   
588 determined by four different methods (Fig. 7). These examples demonstrate a good agree-  
589 ment between the magnetopause proxy based on the mass flux and those obtained by local  
590 methods using both the current density peak and the maximum of the density gradient.  
591 Note that the fluopause is located up to several  $R_E$  further inside the tail.

592 To check the accuracy of the suggested magnetopause proxy, we performed a systematic  
593 comparison with three other methods using all our set of 19 runs for each of three GMHD  
594 models. The scatterplots in the Figure 8 confirm a nice correspondence between all  
595 magnetopause proxies in the terminator ( $X = 0$ ) cross-section both for high- and low-  
596 latitude magnetopause. In the midtail ( $X = -15R_E$ ) the mass flux method is in a good  
597 agreement with both local maxJ and maxgradN methods, while the fluopause appears 1-2  
598  $R_E$  closer to the Sun-Earth line, except for the Open GGCM, which shows comparable  
599 results between all proxies including the fluopause. Note that in the low-latitude midtail  
600 region the gradients of MHD variables are usually too small, so that maxJ and maxgradN  
601 methods become unreliable. For that reason, at  $X = -15R_E$  we use only the high-latitude  
602 portions of the magnetopause in the comparison.

603 Based on the above results, we chose in this study the mass flux reduction method to  
604 identify the magnetopause, which is local, computationally cheap, yields a smooth and  
605 well-defined surface at both high and low latitudes, and agrees quite well with the other  
606 local methods.

607 Once the magnetopause position is determined, it is easy to calculate the tail mag-  
608 netic flux by integrating Bx over the area bounded by the magnetopause. Separation

609 of the magnetic fluxes belonging to the northern/southern lobes was done according to  
610 the positive/negative sign of  $Bx$  (in the GSM system). The magnetopause contour was  
611 then approximated by a spline, and contributions from the boundary cells were taken into  
612 account.

## Appendix B: Empirical data characterising the substorm growth phase parameters

613 The procedure to find the GP parameters was, briefly, as follows (more details will be  
614 published elsewhere). First, we performed a global search of 5 min. averaged OMNI  
615 data for years 2001-2014 to identify the events which had  $> 1.5$  hours northward IMF  
616 ( $Bz > 0.5$  nT, up to two records with data gaps or spikes were allowed) followed by  
617  $> 1.5$  h southward IMF ( $Bz < -0.5$  nT). From them we deleted events that had a  
618 continued activity ( $AL < -100$  nT) throughout the interval, as well as those which had  
619 no distinct  $PC$ -index enhancement associated with the southward IMF turning. The  
620 data selection resulted in 218 events with clear  $PC$ -index onsets, which were assumed as  
621 the actual onsets of convection enhancement in the magnetosphere, that is - the growth  
622 phase onsets. For them we scanned the SuperMAG substorm onset data base [Newell  
623 and Gjerlov, 2011] and found 122 SuperMAG onsets on the nightside available for our  
624 study of growth phase duration as a function of the solar wind merging electric field  
625  $E_{KL}$ . In 90 cases there were no SuperMAG onsets available (more than half of them were  
626 weak events), and 6 cases were discarded as wrong, because of dayside location of the  
627 determining station. The range and distribution of the observed  $T_{GP}$  values as well as  
628 their decreasing trend with the increasing  $E_{KL}$  magnitude are similar to those found in

629 previous studies [*Dmitrieva and Sergeev*, 1983; *Petrukovich*, 2000; *Li et al.*, 2013] and was  
 630 used for testing the simulation results in Section 3 (Fig. 3a).

631 Determination of the tail lobe magnetic field increase and of the loading rate is more  
 632 involved, and no reliable statistical results were published previously on the solar wind  
 633 dependence of these parameters, except for *Rybalchenko and Sergeev* [1985] study, based  
 634 on a small statistics. For that purpose, we used 1-min. resolution Cluster data at distances  
 635 between -9 and -20  $R_E$  and Geotail data at  $r < 25R_E$ , in which only low-beta samples  
 636 ( $2\mu_0 P/B^2 < 0.5$ ) were selected for the analysis, and the equivalent lobe magnetic field was  
 637 defined as ( $B_L = (B^2/2\mu_0 + P)^{1/2}$ ). Alternatively, a similar estimate,  $B_{ext}$ , based on the  
 638 external  $B$ -field part (that is, with the IGRF contribution subtracted) was also computed,  
 639 to avoid some interpretational difficulties in the inner magnetosphere (at  $r < 12R_E$ ). Both  
 640  $B_L$  and  $B_{ext}$  were statistically analyzed in the same way (and the results were found to  
 641 be similar). The next (difficult) task was to obtain the desired statistical dependence of  
 642  $\Delta B_L$  (and  $\Delta B_L/\Delta T$ ) on the solar wind merging  $E$ -field by cleaning the  $B_L$  dependence  
 643 on radial distance and on the solar wind flow pressure, using in both cases the statistical  
 644 dependences derived by *Fairfield and Jones* [1996] (FJ96). First of all, we corrected the  
 645 radial dependence effect by scaling  $B_L$  to  $r = 15R_E$ , based on spacecraft distance and  
 646 using eq. (3) of FJ96. To correct for the changes in solar wind dynamical pressure  $Pd$ ,  
 647 we computed the 5 min. average lobe fields at  $r = 15R_E$  for the OMNI-based  $Pd$  values  
 648 (delayed by 5 min. to account for the solar wind propagation to  $X = -15R_E$ ) based on  
 649 FJ96 formula. The difference of these values (taken at the end and start of time interval  
 650  $\Delta T$  used to compute the loading rate) were then subtracted from the corresponding lobe  
 651 field difference  $\Delta B_L$  to get the corrected lobe change amplitude  $\Delta B_L^{cr}$  and the loading rate

652  $\Delta B_L^c / \Delta T$ . This is what we used for comparison with the simulation results in Section 3  
 653 and Figure 3b.

### Appendix C: Magnetic field divergence and magnetic flux mapping in GMHD models

654 The post-processing analysis often includes interpolation of simulated parameter values,  
 655 available only at discrete grid points. Some procedures require massive interpolation of  
 656 initial values, an example being the magnetic field line tracing procedure. Here we discuss  
 657 how big the interpolation errors can be in terms of the  $\text{div}B = 0$  violation and by testing  
 658 the magnetic flux conservation along the magnetic field line tubes.

659 To obtain the field vector at an arbitrary location inside the 3D grid, one has to sepa-  
 660 rately interpolate the values of  $(B_x, B_y, B_z)$  between the nearest nodes, which necessarily  
 661 creates an artificial divergence, even if the original field had  $\text{div}B = 0$ . Indeed, the ex-  
 662 amination of interpolated magnetic fields in randomized points inside the magnetotail  
 663 showed that the divergence, normalized by its highest possible value at the same location,  
 664  $\|\text{div}B\| = \text{div}B / (|\frac{\partial B_x}{\partial x}| + |\frac{\partial B_y}{\partial y}| + |\frac{\partial B_z}{\partial z}|)$ , may often approach plus/minus unity. It means  
 665 that at such points the variation of interpolated magnetic field is heavily contaminated  
 666 by artificial interpolation errors. To assess the importance of the artificial  $\text{div}B \neq 0$  in  
 667 post-processing, and to test if the integration along the field lines could eliminate the  
 668 random errors, we developed two procedures to calculate the loss/gain of the magnetic  
 669 flux (which should be precisely conserved in an ideal case) along a thin magnetic tube.  
 670 The first procedure evaluates the direct contribution of non-zero  $\text{div}B$  to the magnetic  
 671 flux loss, while the second one evaluates the degree of the magnetic flux non-conservation  
 672 by tracing field lines passing through a finite-size closed contour defining a flux tube.



673 Consider a short element  $dl$  of a thin magnetic field line tube with a cross section area  
 674  $dS(l)$ , the local field magnitude  $B(l)$ , and the corresponding flux:

$$F(l) = B(l)dS \quad (\text{A1})$$

675 Note from the outset that the interpolated magnetic field is not assumed hereto be per-  
 676 fectly divergenceless, i.e.  $\text{div}B \neq 0$  and, hence,  $F(l) \neq \text{const}$ . The flux gain along the  
 677 tube element  $dl$  equals  $dF = \text{div}B(l) \cdot dl \cdot dS(l)$ , which, on account of (A1), yields:

$$\frac{dF}{dl} = \frac{F(l)}{B(l)} \text{div}B(l) \quad (\text{A2})$$

678 OR:

$$\frac{d}{dl} \ln F = \frac{\text{div}B(l)}{B(l)} \quad (\text{A3})$$

679 Integrating (A3) between starting point  $L_1$  and arbitrary location  $L_2$  gives:

$$\ln \frac{F_{L1}}{F_{L2}} = \int_{L_1}^{L_2} \frac{\text{div}B(l)}{B(l)} dl \quad (\text{A4})$$

680 or, in terms of the relative flux gain (loss) between  $L_1$  and  $L_2$ :

$$\Delta F = \frac{F_{L1}}{F_{L2}} - 1 = \exp \left( \int_{L_1}^{L_2} \frac{\text{div}B(l)}{B(l)} dl \right) - 1 \quad (\text{A5})$$

681 The examples of  $\text{div}B$  integration using interpolated fields of three GMHD models and  
 682 corresponding changes of magnetic flux along field lines between the tail cross-section at

683  $X = -15R_E$  and the spherical surface with radius  $r = 5R_E$ , are shown in the right column  
 684 of Figure 9.

685 Also, to evaluate the magnetic flux losses along individual field line tubes, we traced  
 686 the field lines from a set of 360 equidistant starting points lying on a circular contour of  
 687 radius  $1R_E$  at the  $X = -15R_E$  cross-section until they reach a sphere of radius  $r = 5R_E$ ,  
 688 concentric with the Earth's surface. The magnetic flux loss factor was calculated as the  
 689 ratio of magnetic flux through the starting contour  $F_{L1}$  to that permeating the ending  
 690 contour  $F_{L2}$ ,  $\Delta F = F_{L1}/F_{L2} - 1$  (Figure 9, left column).

691 Both procedures show large magnetic flux losses (often exceeding 20-30%) which can  
 692 be generated in the extended areas of the tail cross-section (Figure 9), even quite far from  
 693 the magnetopause and thin current sheets. Similar results are systematically observed  
 694 throughout the simulations.

695 Note that we tried two versions of the interpolation procedure (trilinear and tricubic  
 696 interpolation), and both of them yielded virtually identical results. To estimate the accu-  
 697 racy of the interpolation procedures themselves, we substituted the simulated magnetic  
 698 field with a perfectly divergenceless T89 model field [Tsyganenko, 1989], evaluated in the  
 699 nodes of the same uniform 3D interpolation grid with  $0.5R_E$  spacing, resolution, and ap-  
 700 plied the same tracing procedure based on the interpolated T89 field. The calculation  
 701 results are shown in the same format in the top panels of Figure 9. A closer inspection  
 702 reveals that in the T89 case the absolute value of the normalized numerical  $divB$  does  
 703 not exceed  $10^{-3}$  and the magnetic flux is almost perfectly conserved along the flux tubes,  
 704 except in a vicinity of the neutral sheet. A natural conclusion is that simple interpolation  
 705 procedures do not pose any problem in case of smooth magnetic field distributions (like

706 those in T89), but may result in uncontrolled large errors in the presence of sharp field  
707 gradients.

708 As a consequence, the non-zero divergence of interpolated magnetic fields can signifi-  
709 cantly distort the post-processing calculations in the first-principle based models [*Mackay*  
710 *et al.*, 2001] and especially of those characteristics that involve the field line tracing, such  
711 as the computations of the polar cap area, magnetic tube volume and entropy, magnetic  
712 field line mapping in the magnetosphere and to the ionosphere, etc.

713 Final evaluation of the importance of discovered problems as well as their solution  
714 require a concerted effort on the part of developers, CCMC staff, and the users community.

## References

- 715 Angelopoulos, V., A. Runov, X.-Z. Zhou, D. L. Turner, S. A. Kiehas, S.-S. Li, I. Shinohara  
716 (2013), Electromagnetic energy conversion at reconnection fronts, *Science*, *341*, 1478,  
717 doi:10.1126/science.1236992
- 718 Ashour-Abdalla, M., G. Lapenta, R. J. Walker, M. El-Alaoui, and H. Liang (2015), Mul-  
719 tiscale study of electron energization during unsteady reconnection events, *J. Geophys.*  
720 *Res.*, *120*, 4784–4799, doi:10.1002/2014JA020316.
- 721 Baker, D. N., T. I. Pulkkinen, V. Angelopoulos, W. Baumjohann, and R. L. McPherron  
722 (1996), The neutral line model of substorms: Past results and present view, *J. Geophys.*  
723 *Res.*, *101*, 12975–13010.
- 724 Birn, J., A. Artemyev, D. Baker, M. Echim, M. Hoshino, and L. Zelenyi (2012), Particle ac-  
725 celeration in the magnetotail and aurora, *Space Science Rev.*, *167*, doi:10.1007/s11214-  
726 012-9874-4.

- 727 Clausen, L. B. N., S. E. Milan, J. B. H. Baker, J. M. Ruohoniemi, K.-H. Glassmeier,  
728 J. C. Coxon, and B. J. Anderson (2013), On the influence of open magnetic flux on  
729 substorm intensity: ground- and space-based observations, *J. Geophys. Res.*, *118*, 2958–  
730 2969, doi:10.1002/jgra.50308.
- 731 Clausen, L. B. N., S. E. Milan, and A. Grocott (2014), Thermospheric density per-  
732 turbations in response to substorms, *J. Geophys. Res.Space Physics*, *119*, 44414455,  
733 doi:10.1002/2014JA019837.
- 734 Cowley, S. W. H., and M. Lockwood (1992), Excitation and decay of solar wind driven  
735 flows in the magnetosphere–ionosphere system, *Ann. Geophys.*, *10*, 103–115.
- 736 Daldorff, L. K., G. Tóth, T. I. Gombosi, G. Lapenta, J. Amaya, S. Markidis, and  
737 J. U. Brackbill (2014), Two-way coupling of a global Hall magnetohydrodynamics model  
738 with a local implicit particle-in-cell model, *J. Comput. Phys.*, *268*, 236–254.
- 739 DeJong, A. D., X. Cai, C. R. Clauer, and J. F. Spann (2007), Aurora and open mag-  
740 netic flux during isolated substorms, sawteeth, and SMC events, *Ann. Geophys.*, *25*,  
741 18651–18666.
- 742 DeJong, A. D., A. J. Ridley, X. Cai, and C. R. Clauer (2009), A statistical study of BRIs  
743 (SMCs), isolated substorms, and individual sawtooth injections, *J. Geophys. Res.*, *114*,  
744 A08215, doi:10.1029/2008JA013870.
- 745 Dmitrieva, N.P. and V. A. Sergeev (1983). Spontaneous and induced beginning of the burst  
746 phase of a magnetospheric substorm and its preliminary phase duration, *Geomagnetizm*  
747 *I Aeronomiya*, *23.3*: 470-474, in Russian.
- 748 Dmitrieva, N.P., V. A. Sergeev, M. A. Shukhtina (2004), Average characteristics of the  
749 midtail plasma sheet in different dynamic regimes of the magnetosphere, *Ann. Geophys.*,

750 22, 1432.

751 Dungey, J. W. (1961), Interplanetary magnetic fields and the auroral zones, *Phys. Rev.*  
752 *Lett.*, 6, 47–48.

753 Fairfield, D. H., and J. Jones (1996), Variability of the tail lobe field strength, *J. Geophys.*  
754 *Res.*, 101(A7), 7785–7791, doi:10.1029/95JA03713.

755 Garcia, K. S., and W. J. Hughes (2007), Finding the Lyon-Fedder-Mobarrymagnetopause:  
756 A statistical perspective, *J. Geophys. Res.*, 112, A06229, doi:10.1029/2006JA012039.

757 Gkioulidou, M., A. Y. Ukhorskiy, D. G. Mitchell, T. Sotirelis, B. H. Mauk, and L. J.  
758 Lanzerotti (2014), The role of small-scale ion injections in the buildup of Earth’s ring  
759 current pressure: Van Allen Probes observations of the 17 March 2013 storm, *J. Geo-*  
760 *phys. Res. Space Physics*, 119, 73277342, doi:10.1002/2014JA020096.

761 Goodman, M. L. (1995), A three-dimensional, iterative mapping procedure for the im-  
762 plementation of an ionosphere-magnetosphere anisotropic Ohm’s law boundary con-  
763 dition in global magnetohydrodynamic simulations, *Ann. Geophys.*, 13, 843–853,  
764 doi:10.1007/BF00585-995-0843-z.

765 Gordeev, E. I., V. A. Sergeev, T. I. Pulkkinen, and M. Palmroth (2011), Contribution  
766 of magnetotail reconnection to the cross-polarcap electric potential drop, *J. Geophys.*  
767 *Res.*, 116, A08219, doi:10.1029/2011JA016609.

768 Gordeev, E., V. Sergeev, I. Honkonen, M. Kuznetsova, L. Rastatter, M. Palmroth, P.  
769 Janhunen, C. Tóth, J. Lyon, and M. Wiltberger (2015), Assessing the performance of  
770 community-available global MHD models using key system parameters and empirical  
771 relationships, *Space Weather*, 13, doi:10.1002/2015SW001307.

- 772 Honkonen, I., L. Rastatter, A. Grocott, A. Pulkkinen, M. Palmroth, J. Raeder, A.  
773 J. Ridley, and M. Wiltberger (2013), On the performance of global magneto-  
774 hydrodynamic models in the Earth's magnetosphere, *Space Weather*, *11*, 313–326,  
775 doi:10.1002/swe.20055.
- 776 Huang, C. S., A. D. DeJong, and X. Cai (2009), Magnetic flux in the magnetotail and  
777 polar cap during sawteeth, isolated substorms, and steady magnetospheric convection  
778 events, *J. Geophys. Res.*, *114*, A07202, doi:10.1029/2009JA014232.
- 779 Janhunen, P., M. Palmroth, T. V. Laitinen, I. Honkonen, L. Juusola, G. Facsko, and  
780 T. I. Pulkkinen (2012), The GUMICS-4 global MHD magnetosphere-ionosphere cou-  
781 pling simulation, *J. Atmos. Sol. Terr. Phys.*, *80*, 48–59, doi:10.1016/j.jastp.2012.03.006.
- 782 Jaynes, A. N., et al. (2015), Source and seed populations for relativistic electrons:  
783 Their roles in radiation belt changes, *J. Geophys. Res. Space Physics*, *120*, 72407254,  
784 doi:10.1002/2015JA021234.
- 785 Kuznetsova, M. M., M. Hesse, L. Rastätter, A. Taktakishvili, G. Tóth, D. L. De Zeeuw, A.  
786 Ridley, and T. I. Gombosi (2007), Multiscale modeling of magnetospheric reconnection,  
787 *J. Geophys. Res.*, *112*, A10210, doi:10.1029/2007JA012316.
- 788 Li, H., C. Wang, and Z. Peng (2013), Solar wind impacts on growth phase duration  
789 and substorm intensity: A statistical approach, *J. Geophys. Res.*, *118*, 4270–4278,  
790 doi:10.1002/jgra.50399.
- 791 Lyon, J. G., J. A. Fedder, and C. M. Mobarry (2004), The Lyon-Fedder-Mobarry (LFM)  
792 global MHD magnetospheric simulation code, *J. Atmos. Sol. Terr. Phys.*, *66*(15–16),  
793 1333–1350, doi:10.1016/j.jastp.2004.03.020.

- 794 Mackay, F., R. Marchand, and K. Kabin (2006), Divergence-free magnetic field inter-  
795 polation and charged particle trajectory integration, *J. Geophys. Res.*, *111*, A06205,  
796 doi:10.1029/2005JA011382.
- 797 McPherron, R. L. (1991), Physical Processes Producing Magnetospheric Substorms and  
798 Magnetic Storms, *Geomagnetism*, vol. 4, J. Jacobs, Academic Press Ltd., London, Eng-  
799 land.
- 800 Merkin, V. G., and J. G. Lyon (2010), Effects of the low-latitude ionospheric  
801 boundary condition on the global magnetosphere, *J. Geophys. Res.*, *115*, A10202,  
802 doi:10.1029/2010JA015461.
- 803 Milan, S. E., G. Provan, and B. Hubert (2007), Magnetic flux transport in the Dungey  
804 cycle: A survey of dayside and nightside reconnection rates, *J. Geophys. Res.*, *112*,  
805 A01209, doi:10.1029/2006JA011642.
- 806 Milan, S. E., Grocott, A., Forsyth, C., Imber, S. M., Boakes, P. D., and Hubert, B. (2009),  
807 A superposed epoch analysis of auroral evolution during substorm growth, onset and  
808 recovery: open magnetic flux control of substorm intensity, *Ann. Geophys.*, *27*, 659–668,  
809 doi:10.5194/angeo-27-659-2009.
- 810 Nakamura, T., L. F. Bargatze, T. Mukai, T. Nagai, K. B. Baker, M. R. Hairston,  
811 P. H. Reiff, A. A. Petrukovich, M. Nozdrachev, and O. A. Troshichev (1999), Response  
812 of the midtail electric field to enhanced solar wind energy input, *J. Geophys. Res.*, *104*,  
813 17299–17310, doi:10.1029/1999JA900166.
- 814 Newell, P. T., and J. W. Gjerloev (2011), Substorm and magnetosphere characteristic  
815 scales inferred from the SuperMAGauroralelectrojet indices, *J. Geophys. Res.*, *116*,  
816 A12232, doi:10.1029/2011JA016936.

- 817 Palmroth, M., T. I. Pulkkinen, P. Janhunen, and C.-C. Wu (2003), Stormtime  
818 energy transfer in global MHD simulation, *J. Geophys. Res.*, *108*(A1), 1048,  
819 doi:10.1029/2002JA009446.
- 820 Pembroke, A., F. Toffoletto, S. Sazykin, M. Wiltberger, J. Lyon, V. Merkin, and P.  
821 Schmitt (2012), Initial results from a dynamic coupled magnetosphere-ionosphere-ring  
822 current model, *J. Geophys. Res.*, *117*, A02211, doi:10.1029/2011JA016979.
- 823 Peng, Z., C. Wang, and Y. Q. Hu (2010), Role of IMF  $B_x$  in the solar wind-magnetosphere-  
824 ionosphere coupling, *J. Geophys. Res.*, *115*, A08224, doi:10.1029/2010JA015454.
- 825 Petrukovich, A. A. (2000), The growth phase: Comparison of small and large substorms,  
826 *Proc. 5th International Conference on Substorms (ICS-5)*, edited by A. Wilson, pp.  
827 9–14, European Space Agency, St. Petersburg, Russia.
- 828 Pilipp, W. G., and G. Morfill (1978), The formation of the plasma sheet  
829 resulting from plasma mantle dynamics, *J. Geophys. Res.*, *83*, 5670–5678,  
830 doi:10.1029/JA083iA12p05670.
- 831 Powell, C. G., P. L. Roe, T. J. Linde, T. I. Gombosi, and D. L. De Zeeuw (1999), A  
832 solution-adaptive upwind scheme for ideal magnetohydrodynamics, *J. Comput. Phys.*,  
833 *154*, 284–309, doi:10.1006/jcph.1999.6299.
- 834 Provan, G., Lester, M., Mende, S. B., and Milan, S. E. (2004), Statistical study of high-  
835 latitude plasma flow during magnetospheric substorms, *Ann. Geophys.*, *22*, 3607–3624,  
836 doi:10.5194/angeo-22-3607-2004.
- 837 Pulkkinen, A. et al. (2011), Geospace environment modeling 2008–2009 chal-  
838 lenge: Ground magnetic field perturbations, *Space Weather*, *9*, S02004,  
839 doi:10.1029/2010SW000600.



- 840 Raeder, J., R. L. McPherron, L. A. Frank, S. Kokubun, G. Lu, T. Mukai, W. R. Paterson,  
841 J. B. Sigwarth, H. J. Singer, and J. A. Slavin (2001), Global simulation of the Geospace  
842 Environment Modeling substorm challenge event, *J. Geophys. Res.*, *106(A1)*, 381395,  
843 doi:10.1029/2000JA000605.
- 844 Raeder, J., D. Larson, W. Li, E. L. Kepko, and T. Fuller-Rowell (2008), OpenG-  
845 GCM simulations for the THEMIS mission, *Space Sci. Rev.*, *141(1-4)*, 535–555,  
846 doi:10.1007/s11214-008-9421-5.
- 847 Rastatter, L., M. M. Kuznetsova, A. Vapirev, A. Ridley, M. Wiltberger, A. Pulkkinen, M.  
848 Hesse, and H. J. Singer (2011), Geospace Environment Modeling 2008–2009 Challenge:  
849 Geosynchronous magnetic field, *Space Weather*, *9*, S04005, doi:10.1029/2010SW000617.
- 850 Russell, C. T. and McPherron, R. L. (1973), The magnetotail and substorms, *Space Sci.*  
851 *Rev.*, *15*, 205–266, doi:10.1007/BF00169321.
- 852 Rybalchenko, V.V. and Sergeev, V.A. (1985), Rate of magnetic flux buildup in the  
853 magnetospheric tail, *Geomagn. Aeronomy (Engl. Transl)*, *25*, 378–385.
- 854 Semenov, V. S., V. A. Sergeev (1981), A simple semi-empirical model for the magneto-  
855 spheric substorm, *Planet. Space Sci.*, *29*, 271–281.
- 856 Seppala, A., M. A. Clilverd, M. J. Beharrell, C. J. Rodger, P. T. Verronen, M. E.  
857 Andersson, and D. A. Newnham (2015), Substorm-induced energetic electron pre-  
858 cipitation: Impact on atmospheric chemistry, *Geophys. Res. Lett.*, *42*, 81728176,  
859 doi:10.1002/2015GL065523.
- 860 Shukhtina, M. A., N. P. Dmitrieva, N. G. Popova, V. A. Sergeev, A. G. Yahnin, and I.  
861 V. Deshpande (2005), Observational evidence of the loading-unloading substorm scheme,  
862 *Geophys. Res. Lett.*, *32*, L17107, doi:10.1029/2005GL023779.

- 863 Shukhtina, M. A., N. P. Dmitrieva, and V. A. Sergeev (2014), On the conditions preced-  
864 ing sudden magnetotail magnetic flux unloading, *Geophys. Res. Lett.*, *41*, 1093–1099,  
865 doi:10.1002/2014GL059290.
- 866 Shukhtina, M. A., E. I. Gordeev, V. A. Sergeev, N. A. Tsyganenko, L. B. N. Clausen,  
867 and S. E. Milan (2016), Magnetotail magnetic flux monitoring based on simultane-  
868 ous solar wind and magnetotail observations, *J. Geophys. Res. Space Physics*, *121*,  
869 doi:10.1002/2016JA022911.
- 870 Siscoe, G. L., and T. S. Huang (1985), Polar cap inflation and deflation, *J. Geophys. Res.*,  
871 *90*, 543–547.
- 872 Siscoe, G. L., G. M. Erickson, B. U. Sonnerup, N. C. Maynard, K. D. Siebert,  
873 D. R. Weimer, and W. W. White (2001), Global role of  $E$  in magnetopause  
874 reconnection: An explicit demonstration, *J. Geophys. Res.*, *106*, 13015–13022,  
875 doi:10.1029/2000JA000062.
- 876 Toffoletto, F., S. Sazykin, R. Spiro, and R. Wolf (2005), Inner magnetospheric  
877 modeling with the Rice Convection Model, *Space Sci. Rev.*, *107(1–2)*, 175–196,  
878 doi:10.1023/A:1025532008047.
- 879 Toth, G., et al. (2012), Adaptive numerical algorithms in space weather modeling, *J.*  
880 *Comput. Phys.*, *231(3)*, 870903.
- 881 Tsyganenko, N. A. (1989), A magnetospheric magnetic field model with a warped tail  
882 current sheet, *Planetary and Space Science*, *37(1)*, 5–20.
- 883 Walach, M. -T., and S. E. Milan (2015), Are steady magnetospheric convection  
884 events prolonged substorms?, *J. Geophys. Res. Space Physics*, *120*, 17511758. doi:  
885 10.1002/2014JA020631.

- 886 Wang, C., J. P. Han, H. Li, Z. Peng, and J. D. Richardson (2014a), Solar wind-  
887 magnetosphere energy coupling function fitting: Results from a global MHD simulation,  
888 *J. Geophys. Res.*, *119*, 6199–6212, doi:10.1002/2014JA019834.
- 889 Wang, C.-P., L. R. Lyons, and V. Angelopoulos (2014b), Properties of low-latitude mantle  
890 plasma in the Earth’s magnetotail: ARTEMIS observations and global MHD predic-  
891 tions, *J. Geophys. Res. Space Physics*, *119*, 72647280, doi:10.1002/2014JA020060.
- 892 Yahnin, A. G., I. V. Despirak, A. A. Lubchich, B. V. Kozelov, N. P. Dmitrieva, M. A.  
893 Shukhtina, and H. K. Biernat (2006), Relationship between substorm auroras and pro-  
894 cesses in the near-Earth magnetotail, *Space Sci. Rev.*, *122*, 97106, doi:10.1007/s11214-  
895 006-5884-4.
- 896 Zhang, Q.-H., M. Lockwood, J. C. Foster, S.-R. Zhang, B.-C. Zhang, I. W. McCre-  
897 J. Moon, M. Lester, and J. M. Ruohoniemi (2015), Direct observations of the full  
898 Dungey convection cycle in the polar ionosphere for southward interplanetary magnetic  
899 field conditions, *J. Geophys. Res.*, *120*, 4519–4530, doi: 10.1002/2015JA021172.



**Figure 1.** a) Illustration of basic variables ( $F_T$ ,  $\Phi_{PS}$  and  $\Phi_{MP}$ ) calculated in the  $YZ$  tail cross-section which help to characterize the global flux transfer; b) example of current density distribution in the simulated tail cross-section at  $X = -15R_E$  (color) in LFM simulation; three curves show the magnetopause position obtained by different methods including fluopause (white), as well based on mass flux (black) and density gradient (magenta). Note a good agreement between mass flux and density- and current-based local magnetopause determinations, and that the fluopause stays inward from other proxies by  $1-2R_E$ .



**Figure 2.** Example of solar wind input (set #3 and #8) and comparisons of outputs of three GMHD models; shown are the global magnetospheric parameters cross-polar cap potential, tail magnetic flux and cross-tail potential at  $X = -15R_E$ .

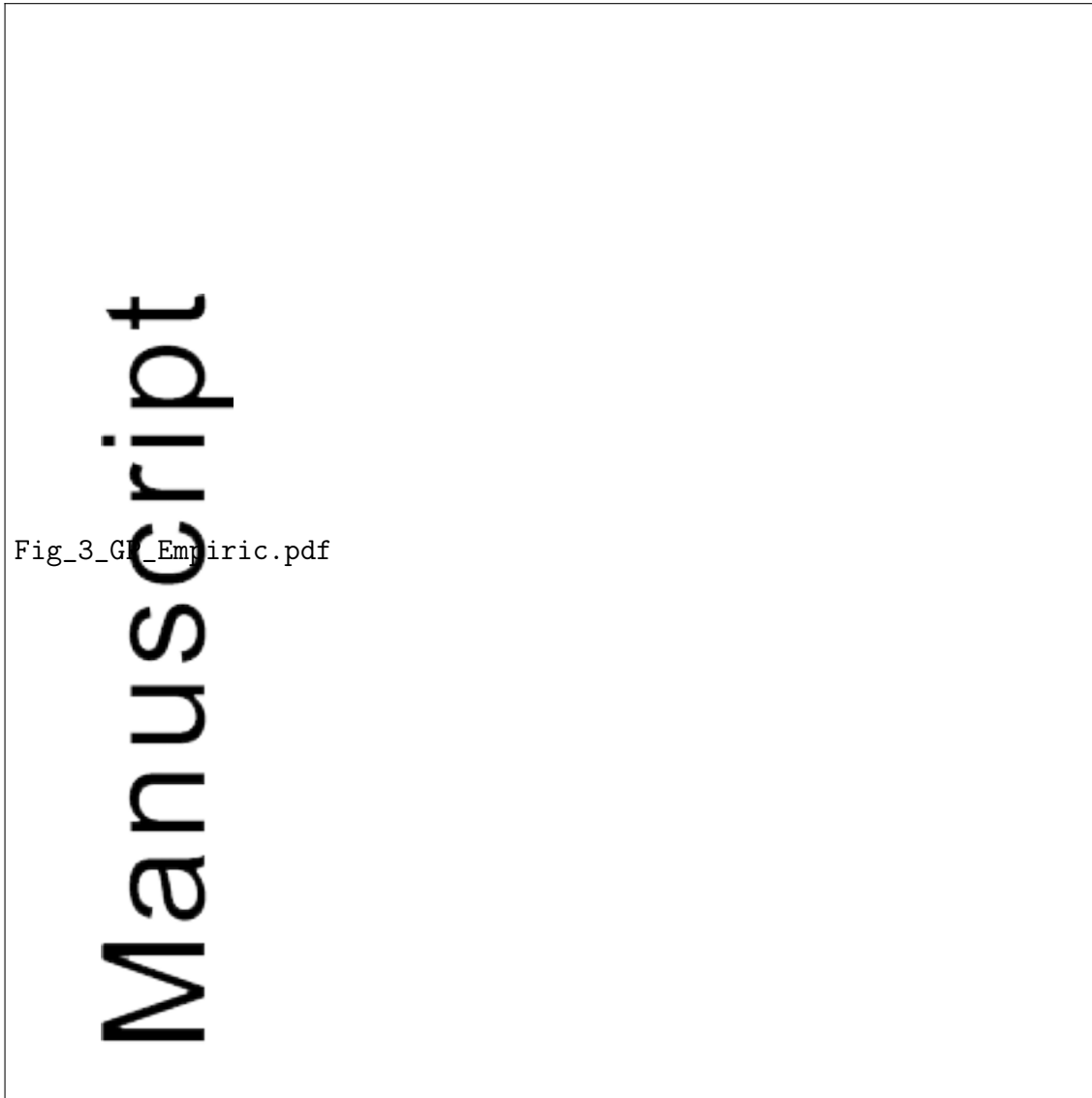


**Figure 3.** Analysis of the growth phase duration (a) and lobe magnetic field loading rate (b) as a function of the merging electric field  $E_{KL}$  in three GMHD models compared with the empirical data. Grey points show the spread of individual events, black stars indicate the derived average values, black lines in (b) correspond to the average linear slope in the observation-based relationships.



Fig\_4\_F\_CTP\_epoch.pdf

**Figure 4.** Superposed epoch analysis of tail magnetic flux (left) and cross-tail potential (right) behavior in three GMHD models.  $T = 0$  epoch corresponds to the beginning of  $F_T$  unloading.

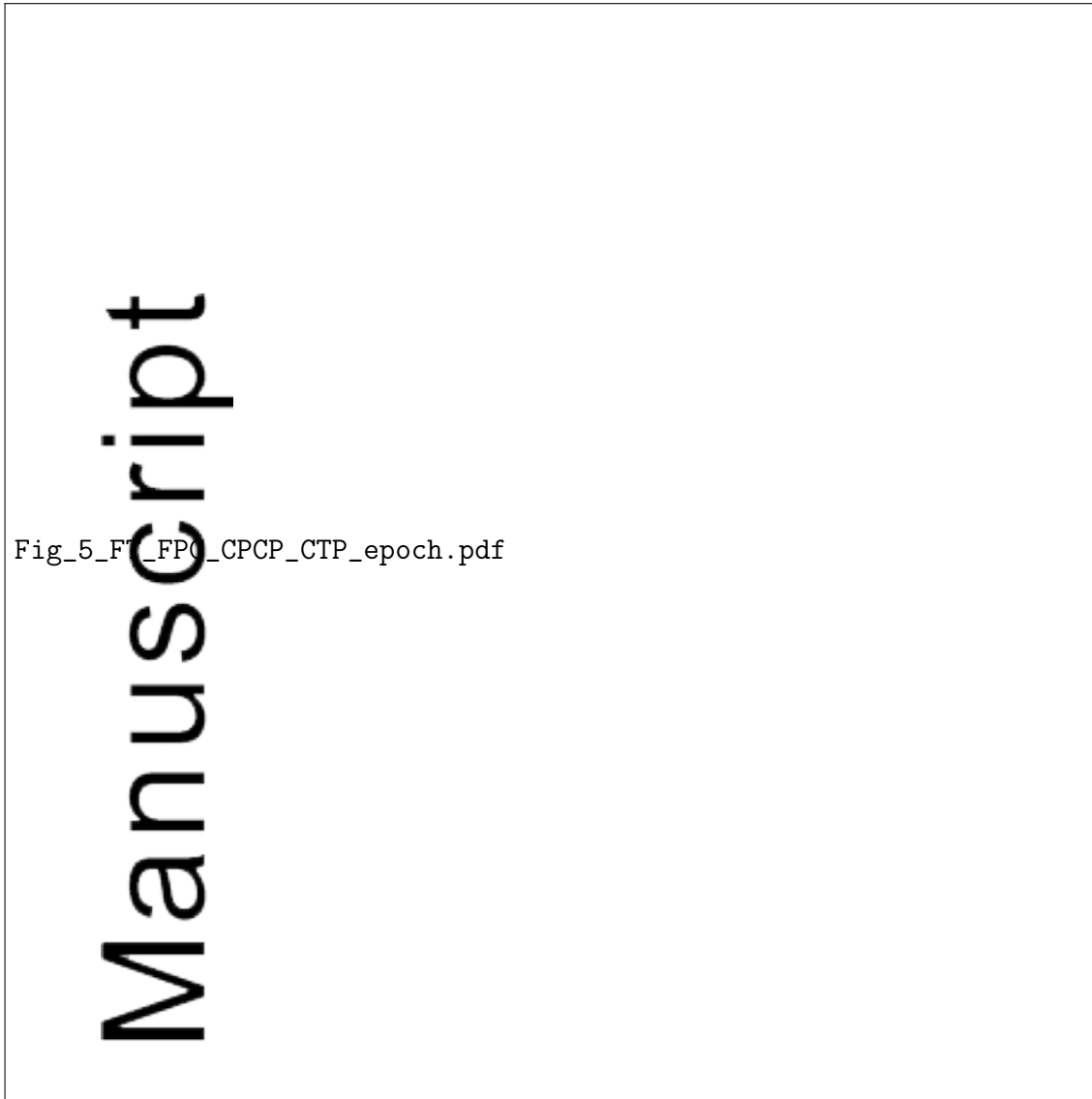


**Figure 5.** Superposed epoch analysis (from left to right) of: tail magnetic flux, polar cap magnetic flux, cross-polar cap potential and cross-tail potential.  $T = 0$  epoch corresponds to the beginning of  $F_T$  unloading.





**Figure 6.** Comparison of integral parameters obtained in simulation #02 with: (Left) overview (medium) and high spatial grid resolution, (Right) - flat and "Auroral conductivity" model.

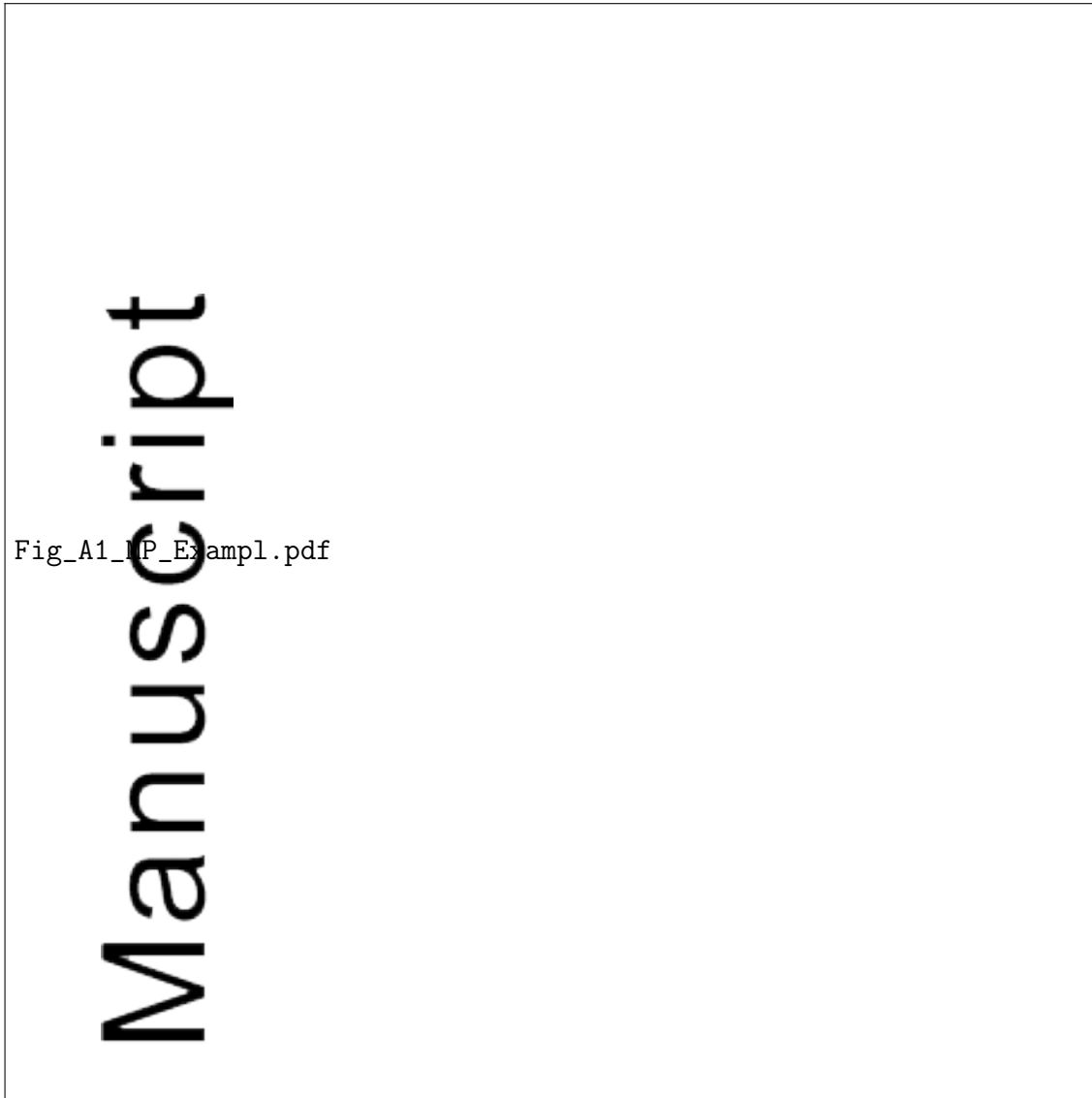


**Figure 7.** Examples of comparing four methods to define the magnetopause in BATS-R-US (a), Open GGCM (b) and LFM (c) simulation, including the current density peak (shown by color distribution), density gradient maximum (magenta), fluopause (white), mass flux (black) methods.



**Figure 8.** Comparison of the magnetopause locations obtained by the mass flux method with those based on the electric current peak (left column) and density gradient (middle column) local methods, as well as with the non-local fluopause method (right column). The scatterplots combine the data at terminator ( $X = 0$ ) and mid-tail ( $X = -15R_E$ ) cross-sections, color-coded for the four magnetopause segments: North (red), South (magenta), Dusk (green) and Dawn (blue). Each  $R_{MP}$  position is calculated as the magnetopause distance averaged over  $15^\circ$  angle.

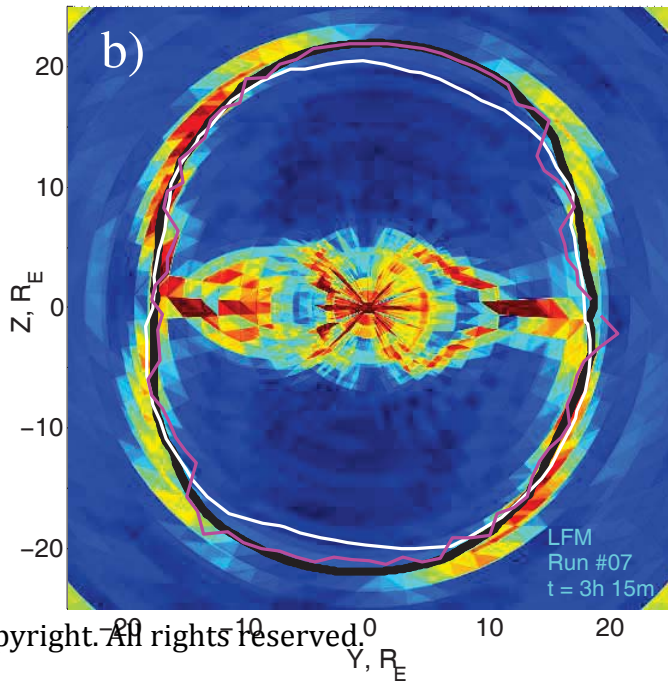
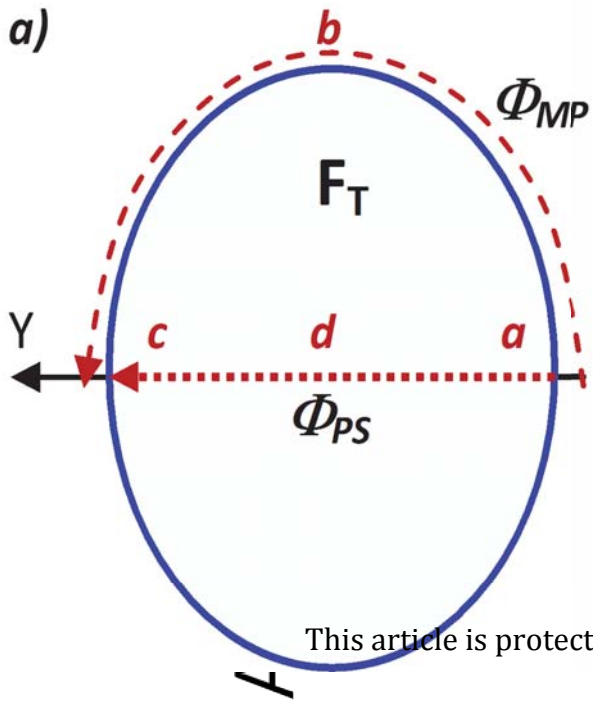


**Figure 9** Color maps of the magnetic flux loss/gain along the tubes from  $X = -15R_E$  cross-section to  $R = 5R_E$  spherical surface calculated by tracing the tubes with  $r = 1R_E$  radius (left column) and integrating of  $divB$  by Eq. (A5) (right column) in CCMC models obtained from results of the #02 runs. Magnetopause contour is shown by thick black line. The maps constructed for the period of substorm expansion. Note the integration does not eliminate the local effects of magnetic flux loss/gain. Note the extended areas of significant magnetic flux loss/gain in BATS-R-US simulations, possibly attributed to disabled  $divB$  elimination during the simulation.

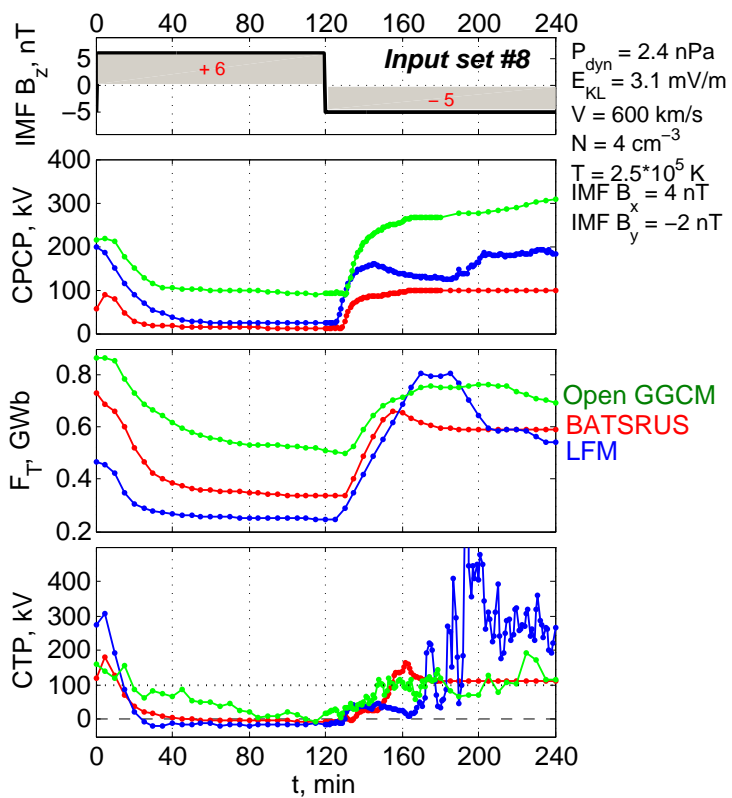
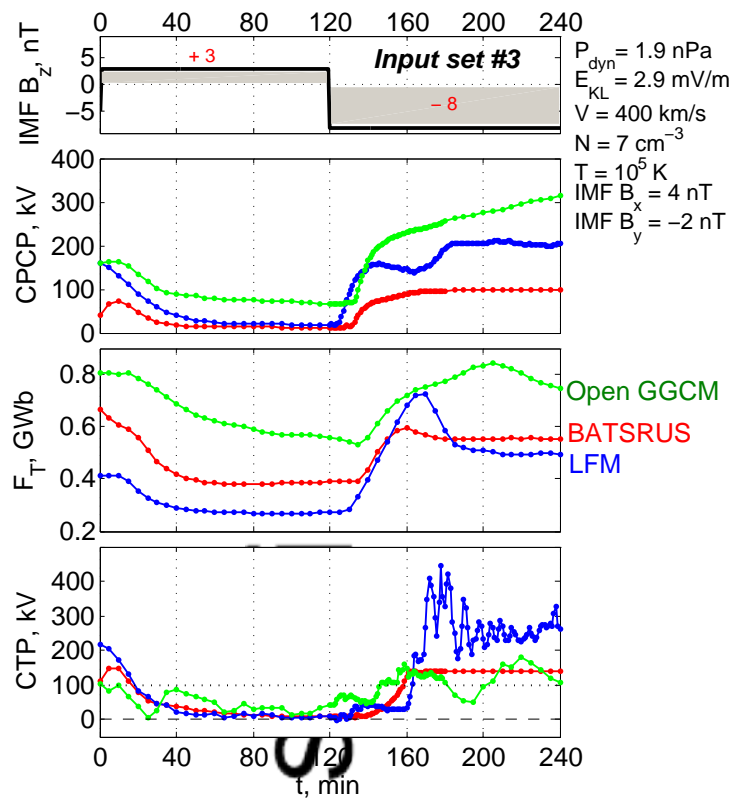
# Author Manuscript

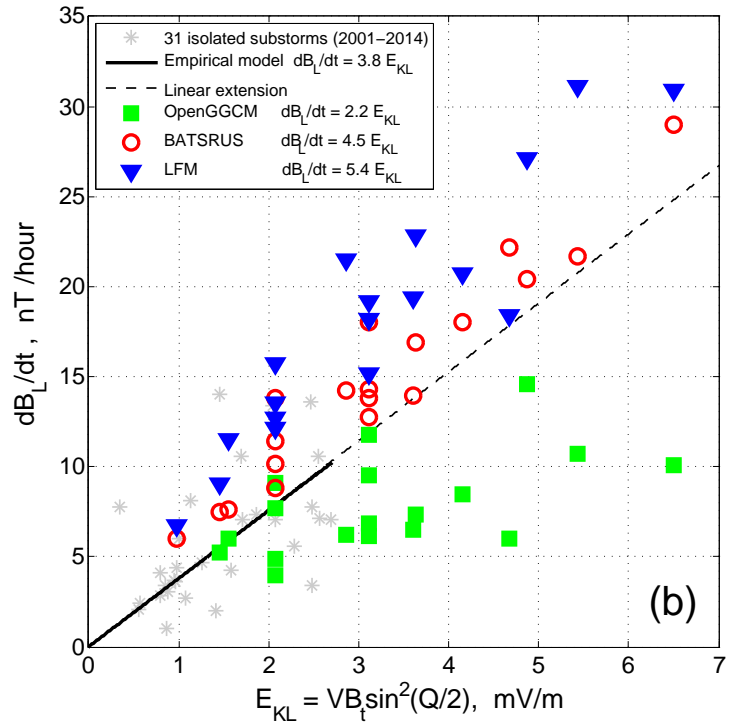
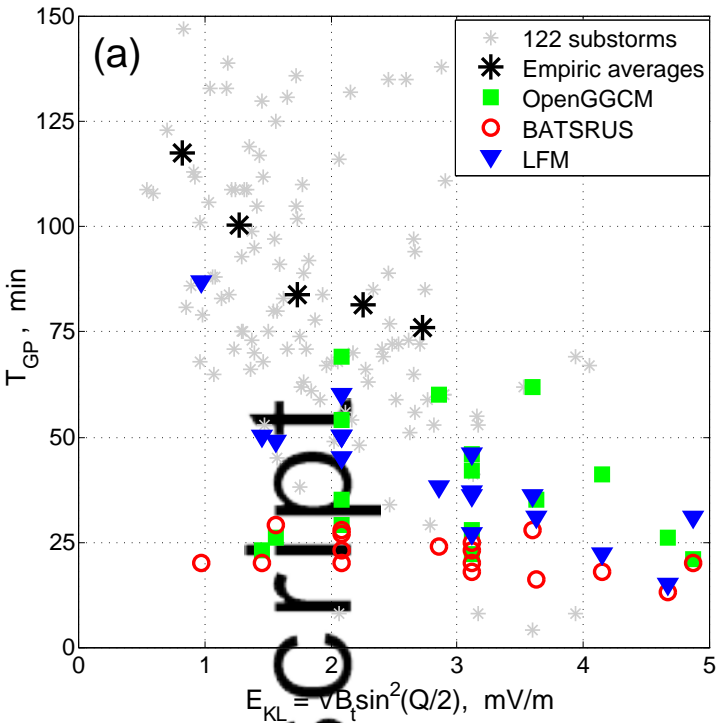
**Table 1.** Average unloading of the magnetotail magnetic flux during the substorm expansion

#	#	F, GWb (onset)	$F_T$ / $F_{PC}$	F, GWb (minimum)	$F_T$ / $F_{PC}$	Normalized unloading amplitude, %	$F_T$ / $F_{PC}$	amplitude, %	$F_T$ / $F_{PC}$	$\Delta t$ , min (unloading duration)	Number of substorms used	Reference
1		0.68		0.47		30%				54	31	[DeJong et al., 2007]
2		0.68		0.50		27%				68	30	[Huang et al., 2009]
3a		0.72		0.50		31%				~80	9	[Milan et al., 2009 (iii-sbs)]
3b		0.86		0.50		42%				~85	10	[Milan et al., 2009 (iv-sbs)]
4		0.82		0.48		41%				60	110	[Shukhtina et al., 2014]
5		0.50		0.40		20%				60	4083	[Walach and Milan, 2015]
6		0.60		0.57		5%				15	19	BATS-R-US (this study)
		0.77		0.75		8%				60	18	Open GGCM (this study)
7		0.77		0.71		8%				60	18	Open GGCM (this study)
		1.10		0.87		31%				50	19	LFM (this study)
8		0.71		0.49		31%				50	19	LFM (this study)
		0.80		0.61		24%				50	19	LFM (this study)

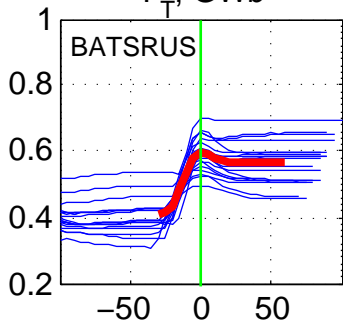


This article is protected by copyright. All rights reserved.

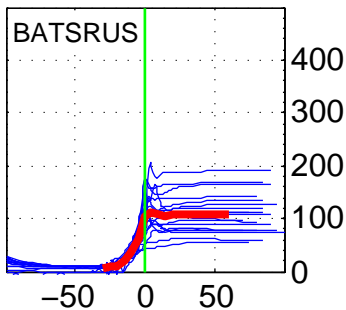




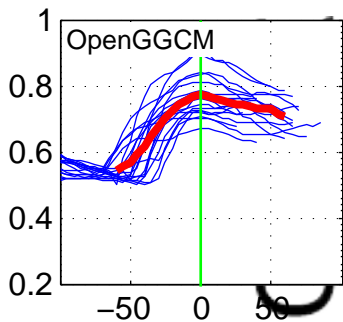


$F_T$ , GWb

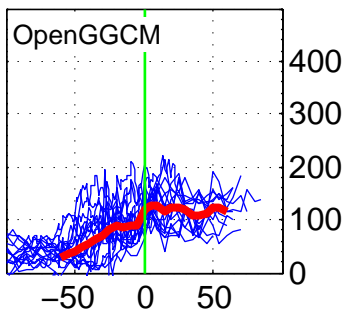
CTP, kV



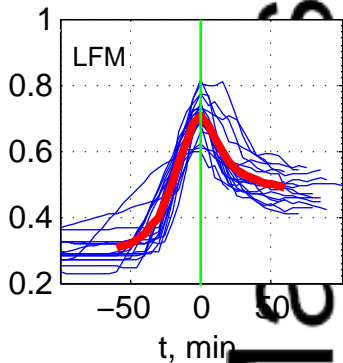
OpenGGCM



OpenGGCM



LFM



LFM

